

## Readout and control of a single nuclear spin with a meta-stable electron spin ancilla

Sang-Yun Lee<sup>1+</sup>, Matthias Widmann<sup>1</sup>, Torsten Rendler<sup>1</sup>, Marcus Doherty<sup>2\*</sup>, Thomas M. Babinec<sup>3,5</sup>, Sen Yang<sup>1</sup>, Moritz Eyer<sup>1</sup>, Petr Siyushev<sup>1</sup>, Birgit J. M. Haussmann<sup>3</sup>, Marko Loncar<sup>3</sup>, Zoltán Bodrog<sup>4</sup>, Adam Gall<sup>4</sup>, Neil Manson<sup>2</sup>, Helmut Fedder<sup>1+\*</sup>, Jörg Wrachtrup<sup>1</sup>

1. *3. Physikalisches Institut and Research Center SCOPE, University Stuttgart, Pfaffenwaldring 57, 70569 Stuttgart, Germany*
2. *Laser Physics Centre, Research School of Physics and Engineering, Australian National University, Canberra, A. C. T., 0200, Australia*
3. *School of Engineering and Applied Science, Harvard University, Cambridge, Massachusetts 02138, USA*
4. *Department of Atomic Physics, Budapest University of Technology and Economics, Budafoki út 8, H-1111, Budapest, Hungary*
5. *Department of Applied Physics, Stanford University, 348 Via Pueblo Mall, Stanford, CA 9430 (current address)*

+These authors contributed equally

\*e-mail: [helmut.fedder@gmail.com](mailto:helmut.fedder@gmail.com)

\*e-mail: [marcus.doherty@anu.edu.au](mailto:marcus.doherty@anu.edu.au)

**Electron and nuclear spins associated with point defects in insulators are promising systems for solid state quantum technology<sup>1-3</sup>. While the electron spin usually is used for readout and addressing, nuclear spins are exquisite quantum bits<sup>4,5</sup> and memory systems<sup>3,6</sup>. With these systems single-shot readout of nearby nuclear spins<sup>5</sup> as well as entanglement<sup>4,7,8</sup> aided by the electron spin has been shown. While the electron spin in this example is essential for readout it usually limits nuclear spin coherence<sup>9</sup>. This has set of the quest for defects with *spin-free* ground states<sup>8,10</sup>. Here, we isolate a hitherto unidentified defect in diamond and use it at room temperature to demonstrate optical spin polarization and readout with exceptionally high contrast (up to 45%), coherent manipulation of an individual excited triplet state spin, and coherent nuclear spin manipulation using the triplet electron spin as a meta-stable ancilla. By this we demonstrate nuclear magnetic resonance and Rabi oscillations of the uncoupled nuclear spin in the spin-free electronic ground state. Our study demonstrates that nuclei coupled to single metastable electron spins are useful quantum systems with long memory times despite electronic relaxation processes.**

Coupled electron and nuclear spins in solids are promising candidates for quantum memories and registers and present a particular class in the emerging field of hybrid quantum systems<sup>7,11-14</sup>, in which different types of qubits perform distinct functions according to their advantageous properties. In this particular case, the nuclear spin, which is weakly coupled to the environment, serves as a long-lived

quantum memory, whereas the electron spin, which has a short coherence time, but interacts strongly with external fields, serves as a readout gate<sup>4,7,9</sup>. In this architecture, the permanent presence of the electron spin is a source of decoherence to the nuclear spin<sup>8</sup>. To avoid such electron spin induced decoherence, the electron that carries the spin should be physically removed when it is not needed and returned to the nuclear spin only when the initialization or readout gate is applied. One approach to address this problem is to frequently remove the electron, e.g. by photo-ionization with a strong laser, resulting in a motional narrowing type of decoupling<sup>9</sup>. Another approach – that is followed in this work – is to choose an electronic system with a spin-free ground state and a meta-stable excited spin state that can be optically pumped and activated prior to the application of the readout gate<sup>8</sup>. Such a system implemented with a single solid state defect would enable a universal nuclear spin gate. In the following we present a suitable defect in diamond and demonstrate coherent control of a single nuclear spin in the spin-free electronic ground state. Notably, besides the NV center, this is the second known single spin defect in the solid state, whose coherent spin motion is detectable at room temperature.

The defect<sup>1</sup> is observed in ultra-pure single crystalline HPHT diamond after fabrication of vertical nano-wires (see Fig. 1a,b), whose main purpose is to provide high photon collection efficiency<sup>15</sup>. The wires are etched into the sample surface by reactive ion etching (see SI). Fig. 1c shows a confocal fluorescence microscope image of the sample. To identify candidates for meta-stable triplet spin defects, we observe the fluorescence intensity of bright spots on the sample surface with and without a strong applied magnetic field from a permanent magnet ( $\approx 0.5$  T) (see Fig. 1d). An arbitrary oriented magnetic field causes spin mixing and thereby modifies the steady-state fluorescence<sup>16</sup>. We observe two types of emitters with decreasing and increasing fluorescence response, corresponding to NV<sup>-</sup> centers and the new ST1 defects, respectively. The increase of the steady-state fluorescence is due to the mixing of meta-stable triplet states as will be shown later.

To characterize the defect further, we record the photon auto-correlation and observe a dip well below 0.5 at zero delay, which confirms that we indeed observe single defects<sup>17</sup> (see Fig. 1g). At higher excitation intensity, the photon auto-correlation shows pronounced ‘bunching-shoulders’, which supports the idea of the existence of a long-lived shelving state. To characterize the defect fluorescence, we present fluorescence emission spectra at room-temperature and at 10K (see Fig. 1e). In both cases a strong resonant emission line is observed at 550(1) nm, with a broad phonon side band extending to the near infrared. Notably, this resonant transition does not correspond to a known diamond defect line<sup>18</sup>. To characterize the strength of the optical transition, we present the excited state lifetime that we have determined in a room temperature experiment by pulsed optical excitation (see Fig. 1f). An excited state lifetime of 9.5(2) ns is observed.

Next, we search for a signature of an electron spin resonance in the optical fluorescence. Fig. 2a shows the fluorescence intensity that is observed while sweeping the microwaves from 200 to 1400 MHz. Three distinct lines marking an increase in fluorescence intensity upon spin resonance are observed at frequencies  $2E = 278(1)$  MHz,  $D-E=996(1)$  MHz,  $D+E=1274(1)$  MHz. This optically detected magnetic resonance (ODMR) spectrum indicates a triplet electron spin with zero field splitting parameters<sup>19</sup>

---

<sup>1</sup> hereafter termed ST1-defect following the convention that is commonly applied in the EPR community

$D=1135(1)$  MHz and  $E=139(1)$  MHz. The observed large  $E$  parameter could originate from the presence of a large local strain or from an intrinsic low symmetry of the defect. We have compared the spin resonance spectra of  $\sim 20$  individual defects (see SI) and observed variations of the  $E$  parameter smaller than 5 MHz, indicating that the  $E$  originates from an intrinsic low symmetry of the defect. From ODMR spectra with a variable axial magnetic field applied (Fig. 2b), we determine an electronic  $g$ -factor  $g_e = 2.0(1)$ , close to the  $g$ -factor of the free electron spin. The absence of an intrinsic hyperfine splitting indicates that the defect's constituent atoms possess no nuclear spin (see SI for a detailed discussion of the possible constituents and structure of the defect). The aligned axial magnetic field has an angle of  $35(1)^\circ$  w.r.t the [111] crystal direction, indicating that the defect's main symmetry axis is oriented along the [110] crystal direction (see inset in Fig. 2b).

All findings reported up to here are compatible with two possible electronic configurations: the triplet state could either be the long lived shelving state or the ground state. To show that the triplet state is indeed the long lived shelving state, we measure the decay of the shelving state population. If the shelving state was a singlet, a single exponential decay would be expected. By contrast, in the present case, three distinct exponential decay terms are observed (Fig. 3b) and their amplitudes are sensitive to microwave fields resonant with the triplet ESR transitions. In each decay curve shown, the dominant decay terms are controlled by switching the spin population with microwave  $\pi$ -pulses resonant with the three ESR transitions. This indicates that the shelving state is indeed the triplet state. The result can be used to assign the decay constants to the spin quantum numbers (Fig. 3c). A complete model of the optical cycle can be established by determining also the triplet population rate by an analogous pulsed experiment (see SI). Fig. 3d summarizes all results related to the triplet kinetics. The essential features are: a rapid ( $\sim 1/70$  ns) inter-system-crossing rate from the singlet excited state to the triplet state and substantial differences among the triplet lifetimes,  $\tau_{|0\rangle} \approx 2500$  ns,  $\tau_{|-1\rangle} \approx 1000$  ns,  $\tau_{|+1\rangle} \approx 200$  ns. These are responsible for the positive and exceptionally high (45 %) optical spin signal contrast, and increasing steady-state fluorescence response to a randomly aligned static magnetic field as observed in Fig. 1d because mixing the triplet sublevels results in faster decay to the ground state. It follows that optical pumping prepares the system in a spin polarized state of the meta-stable triplet state with predominant population of the slowly decaying triplet sublevel,  $|0\rangle$ . We now apply coherent spin manipulation to demonstrate Rabi oscillations between the triplet spin states (Fig. 4). Because the spin population of the faster decaying states  $|+\rangle$  or  $|-\rangle$  is increased by a resonant ESR pulse, any coherent spin manipulation results in the enhancement of the fluorescence intensity as shown in Fig. 4b. The oscillations are described by two exponential decay functions, one of which is modulated by a cosine. The decay times and oscillation amplitudes correspond to the average of the lifetimes and the difference of the initial populations of the two involved spin states, respectively, and are in excellent agreement with the rates measured independently above (Fig. 3d). Note that the decay times are fully accounted for by the triplet lifetimes, which implies that spin relaxation is negligible. The triplet lifetimes are long enough to coherently address a coupled nuclear spin. We have compared the Zeeman sweeps of about 20 defects and observe that two of them show hyperfine splittings due to proximal  $I = 1/2$  carbon nuclear spins of several tens of MHz see (Fig. 5a).

We now show the application of the metastable electron spin as a universal single nuclear spin gate and demonstrate coherent manipulation and readout of the nuclear spin in the spin-free electronic ground state. To achieve this, we exploit the metastable electronic triplet spin ancilla to transfer spin-polarization onto and off the nuclear spin. To this end we exploit the optical nuclear polarization (ONP) induced by a level-anti-crossing (LAC) between the  $| -1, +1/2 \rangle$  and  $| 0, -1/2 \rangle$  hyperfine levels at about 42 mT to selectively mix electronic and nuclear spin states<sup>2020</sup> (see SI). Under these conditions, spin-polarization is transferred to the nuclear spin when the electron enters the meta-stable triplet level resulting in optical polarization of the nuclear spin<sup>21</sup>. After the optical pump pulse is turned off, the electron decays to the singlet ground state within a time given by the triplet lifetime. This decay eliminates the triplet electron spin and leaves the nuclear spin in its polarized state. Likewise, when the system is optically pumped from the singlet ground state to the excited triplet state, the nuclear spin state is preserved and the hyperfine levels are populated correspondingly. At the LAC, the different lifetimes of the hyperfine levels result in different fluorescent intensity of the nuclear spin projections. This provides a mechanism to readout the nuclear spin (see Fig. 5b and Methods). Fig. 5c shows the nuclear spin signal contrast as the energy levels are tuned into the LAC. Nuclear spin polarization is maximal at the LAC and vanishes when the detuning from the LAC becomes comparable to the hyperfine coupling strength. As an application of the nuclear spin manipulation, we show nuclear magnetic resonance (NMR) and coherent manipulation of the nuclear spin via Rabi oscillations (Fig. 5 d,e). For the measurement of a nuclear magnetic resonance spectrum, we apply a radio-frequency (RF)  $\pi$ -pulse of variable frequency. We observe a resonance dip at 450(1) kHz, corresponding to the Larmor precession frequency  $\nu_{13C} = \gamma_{13C} B = 447.5$  kHz of a bare  $^{13}\text{C}$  nucleus. Here,  $\gamma_{13C} = 10.705$  kHz/mT is the gyromagnetic ratio of the  $^{13}\text{C}$  nuclear spin and  $B = 41.8(5)$  mT is the applied field (corresponding to the LAC). We can thereby identify the coupled nuclear spin as a  $^{13}\text{C}$  lattice spin. Note the absence of a chemical shift which indicates that indeed the electron spin is absent. For the measurement of nuclear Rabi oscillations, we apply a resonant RF pulse of variable length between the initialization and readout laser pulses. Several Rabi oscillations are observed that decay on a time scale of about 1 ms. The decay is likely to originate from dipole-dipole coupling of the nuclear spin to surrounding  $^{13}\text{C}$  lattice spins. Note that the dominant decay mechanism is spin diffusion. By contrast to ensemble magnetization (that decays with  $T_1$ ), here the relevant time scale is the ensemble  $T_2^*$  time that is about 10 ms in diamond with natural  $^{13}\text{C}$  abundance<sup>22</sup> and agrees reasonably with the observed decoherence time. For future increase of the coherence time, such dipole interactions between nuclei of the same species can be efficiently removed by homonuclear decoupling schemes<sup>9,23-25</sup>. Other sources of decoherence could be paramagnetic or nuclear spin impurities at the surface whose decoherence effects could be avoided by isolating ST1 defects in the bulk crystal.

The defect spin system presented in this work holds promise for room temperature solid state nuclear spin memories and quantum registers with ultra-long spin coherence times. Such a device could be used as a memory in integrated hybrid quantum systems<sup>13,14</sup> or as a solid state quantum token<sup>9</sup>. For such applications, coherence times on the order of seconds or hours are desirable. Owing to its spin-free ground state, the system presented here is a promising candidate for achieving such long coherence times by homonuclear dynamical decoupling, such as BLEW<sup>23</sup>, FSLG<sup>24</sup>, MREV<sup>25</sup>. An increase of the nuclear spin coherence time by several orders of magnitude is expected<sup>9</sup>. In diamond, the coherence

time of  $^{13}\text{C}$  nuclear spins (at room temperature) is ultimately limited to time scales on the order of one day<sup>22</sup>.

## Methods

### Polarization and readout of the triplet spin state

A long intense laser pulse is applied to prepare the system in a spin-polarized state of the triplet level. The intensity and length of the pulse are chosen such that the optical transition is saturated and steady state fluorescence is reached during the pulse. Thereby the majority of the population is transferred to the slowly decaying triplet sublevel, while the two other triplet levels and the ground and excited states are nearly empty. The laser pulse is followed by a short idle time ( $\sim 50$  ns) to allow any residual population of the excited state to decay.

To readout the triplet spin state, the fluorescence is recorded during a laser pulse that is identical to the preparation pulse. Decaying fluorescence response curves are observed that encode the triplet populations. In particular, the fluorescence counts summed over a window at the beginning of the response profiles are proportional to the three triplet spin populations. This fluorescence is plotted in Fig. 3 and 4. In all data shown, a 200 ns integration window was used.

### Polarization and readout of the nuclear spin

The nuclear spin is initialized by applying a long ( $10\ \mu\text{s}$ ) laser pulse (duration longer than several triplet lifetimes) followed by an idle time ( $20\ \mu\text{s}$ ) that ensures that the triplet population is fully decayed to the electronic ground state prior to any nuclear spin manipulation. The readout consists of a second laser pulse with simultaneous detection of the fluorescence, as in the case of the electron spin manipulation, except that now a longer ( $8\ \mu\text{s}$ ) integration window is used to accumulate fluorescence contrast. As before, the integrated fluorescence encodes the spin state.

1. Ladd, T. D. *et al.* Quantum computers. *Nature* **464**, 45–53 (2010).
2. Koehl, W. F., Buckley, B. B., Heremans, F. J., Calusine, G. & Awschalom, D. D. Room temperature coherent control of defect spin qubits in silicon carbide. *Nature* **479**, 84–7 (2011).
3. Morton, J. J. L. *et al.* Solid-state quantum memory using the <sup>31</sup>P nuclear spin. *Nature* **455**, 1085–1088 (2008).
4. Dutt, M. V. G. *et al.* Quantum register based on individual electronic and nuclear spin qubits in diamond. *Science* **316**, 1312–1316 (2007).
5. Neumann, P. *et al.* Single-shot readout of a single nuclear spin. *Science (New York, N.Y.)* **329**, 542–4 (2010).
6. Steger, M. *et al.* Quantum information storage for over 180 s using donor spins in a <sup>28</sup>Si “semiconductor vacuum”. *Science (New York, N.Y.)* **336**, 1280–3 (2012).
7. Neumann, P. *et al.* Multipartite entanglement among single spins in diamond. *Science* **320**, 1326–1329 (2008).
8. Filidou, V. *et al.* Ultrafast entangling gates between nuclear spins using photoexcited triplet states. *Nature Phys.* **8**, 1–5 (2012).
9. Maurer, P. C. *et al.* Room-Temperature Quantum Bit Memory Exceeding One Second. *Science* **336**, 1283–1286 (2012).
10. Akhtar, W. *et al.* Coherent Storage of Photoexcited Triplet States Using <sup>29</sup>Si Nuclear Spins in Silicon. *Phys. Rev. Lett.* **108**, 1–5 (2012).
11. Brennecke, F., Ritter, S., Donner, T. & Esslinger, T. Cavity optomechanics with a Bose-Einstein condensate. *Science (New York, N.Y.)* **322**, 235–8 (2008).
12. Brown, K. R. *et al.* Coupled quantized mechanical oscillators. *Nature* **471**, 196–9 (2011).
13. Zhu, X. *et al.* Coherent coupling of a superconducting flux qubit to an electron spin ensemble in diamond. *Nature* **478**, 221–4 (2011).
14. Kubo, Y. *et al.* Strong Coupling of a Spin Ensemble to a Superconducting Resonator. *Phys. Rev. Lett.* **105**, 1–4 (2010).
15. Babinec, T. M. *et al.* A diamond nanowire single-photon source. *Nature Nanotech.* **5**, 195–9 (2010).
16. Epstein, R. J., Mendoza, F. M., Kato, Y. K. & Awschalom, D. D. Anisotropic interactions of a single spin and dark-spin spectroscopy in diamond. *Nature Phys.* **1**, 94–98 (2005).

17. Kurtsiefer, C., Mayer, S., Zarda, P. & Weinfurter, H. Stable solid-state source of single photons. *Physical review letters* **85**, 290–3 (2000).
18. Zaitsev, A. M. *Optical Properties of Diamond: A Data Handbook*. (Springer: Berlin, 2001).
19. Carrington, A. & McLachlan, A. D. *Introduction to magnetic resonance with applications to chemistry and chemical physics*. (Harper & Row: 1967).
20. Jacques, V. *et al.* Dynamic Polarization of Single Nuclear Spins by Optical Pumping of Nitrogen-Vacancy Color Centers in Diamond at Room Temperature. *Phys. Rev. Lett.* **102**, 7–10 (2009).
21. Colpa, J. P. & Stehlik, D. Optical nuclear polarization as a consequence of the non-crossing rule (level-anti-crossing). *Chemical Physics* **21**, 273–288 (1977).
22. Reynhardt, E. C. & Terblanche, C. J. <sup>13</sup>C relaxation in natural diamond. *Chemical Physics Letters* **269**, 464–468 (1997).
23. Burum, D. ., Linder, M. & Ernst, R. . Low-power multipulse line narrowing in solid-state NMR. *Journal of Magnetic Resonance (1969)* **44**, 173–188 (1981).
24. Bielecki, A., Kolbert, A. C. & Levitt, M. H. Frequency-switched pulse sequences: Homonuclear decoupling and dilute spin NMR in solids. *Chemical Physics Letters* **155**, 341–346 (1989).
25. Rhim, W.-K. Enhanced resolution for solid state NMR. *The Journal of Chemical Physics* **58**, 1772 (1973).

## Acknowledgements

We acknowledge support by the DFG via Forschergruppe 1493 and SFB/TR21 as well as the EU via the ERC grant SQUTEC. B.H. gratefully acknowledges support from HQOC. We thank Matthew Sellars, Phil Hemmer, Philipp Neumann, Roman Kolesov, Rainer Stöhr and Christian Burk for fruitful discussion.

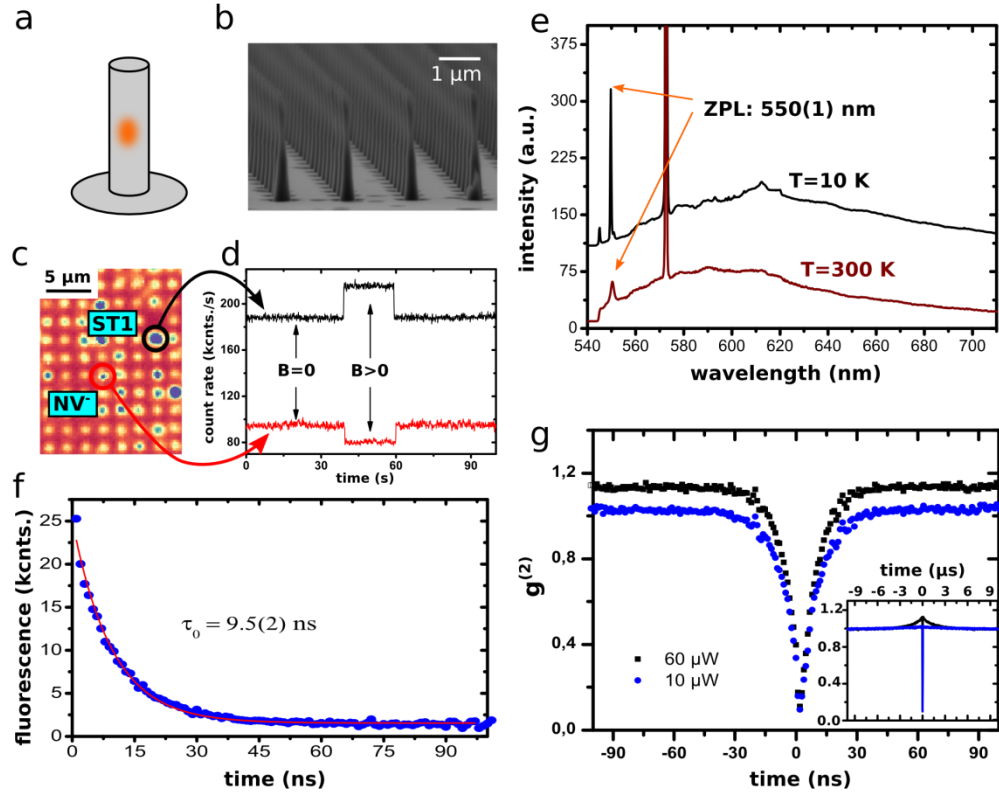


**Fig. 1 | Optical properties of the ST1 defect.** **a**, Illustration of a diamond nano wire containing a single fluorescent point defect. **b**, SEM image of the [111] HPHT diamond sample with fabricated nano wires (diameter  $\sim 200$  nm, length  $\sim 2$   $\mu\text{m}$ ). **c**, confocal fluorescence microscope image of the sample. The marked wires contain single NV $^-$  and ST1 defects. **d**, fluorescence time trace recorded during application and removal of a non-aligned magnetic field. The fluorescence is quenched and enhanced for NV $^-$ , and ST1 defects, respectively. **e**, fluorescence emission spectrum of a single ST1 defect at room temperature and liquid helium temperature. A zero phonon line at 550(1) nm and a broad emission band in the red to NIR range is observed, **f**, fluorescence decay showing an excited state life time of 9.5 ns, **g**, second order photon correlation at increasing excitation power. The dip at delay  $t=0$  reaches well below 0.5, proving the single center nature of the defect. At high excitation power pronounced bunching shoulders are observed, that indicate the presence of a long lived shelving state.

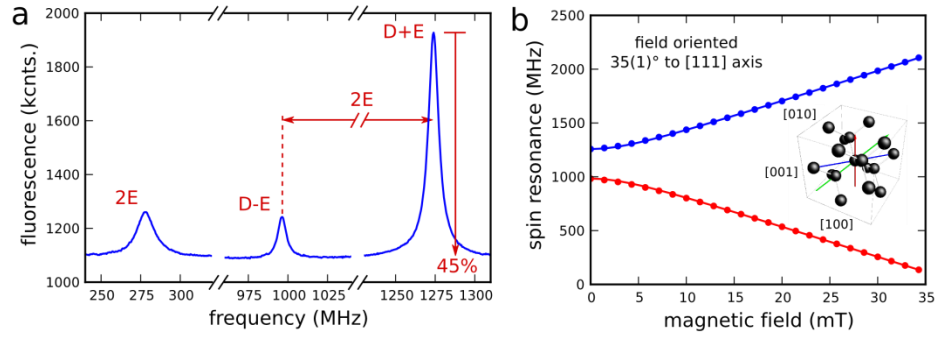


**Fig. 2 | Optically detected electron spin resonance.** **a**, room temperature ESR spectrum at zero magnetic field. Resonant transitions are indicated by their zero-field splitting parameters  $D=1135(1)$  MHz and  $E=139(1)$  MHz. We observe an exceptionally high optical spin signal contrast of the D+E spin projection of about 45 %, **b**, Zeeman curve with an aligned axial magnetic field oriented along the defect main symmetry axis ( $35(1)^\circ$  w.r.t. the [111] crystal axis); dots: experiment, lines: theoretical fit obtained from the triplet spin Hamiltonian  $H = D S_z - S(S + 1)/3 + E S_x - S_y + g S_z B_z$ , where  $S_\alpha$  are the usual spin operators for total Spin  $S = 1$ ,  $g$  is the  $g$ -factor and  $B_z$  is the axial field (see SI). The inset shows a schematic illustration of the crystallographic orientation of the defect. Green, blue and red arrows denote the [111], [110] (defect's main axis) and [001] ( $C_{2v}$  symmetry axis), respectively.

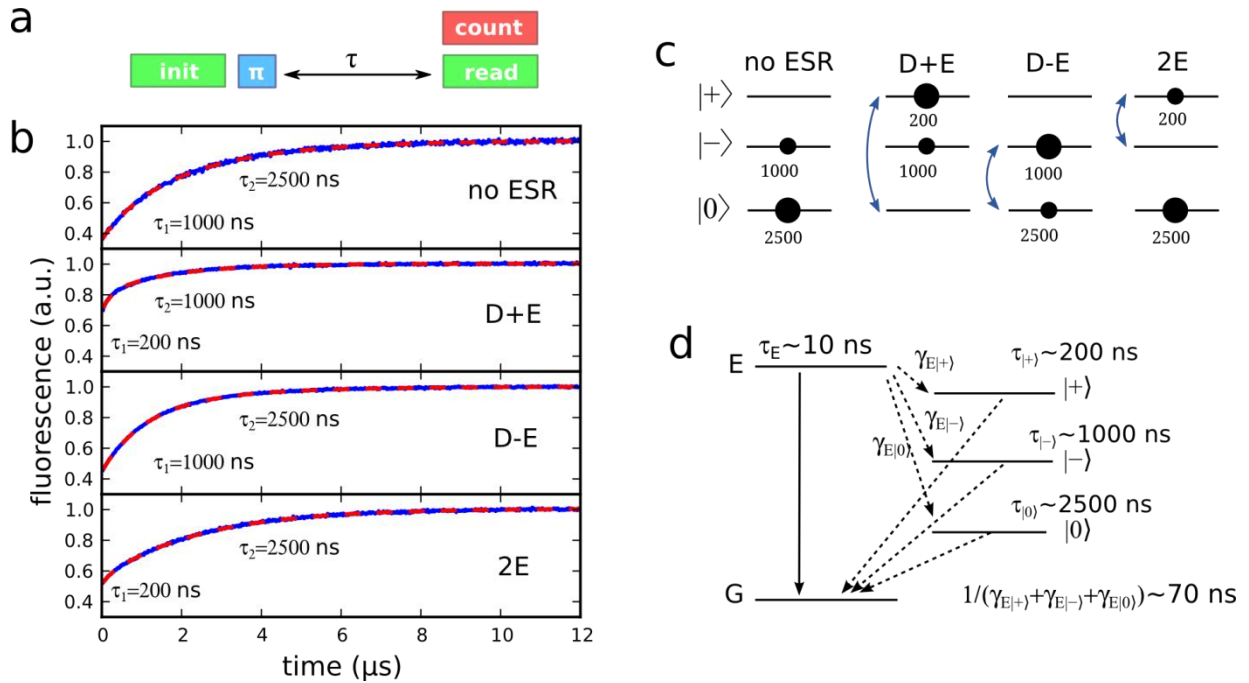


**Fig. 3 | Kinetics of the shelving state and energy level scheme. a**, optical and microwave pulse sequence for the measurement of the shelving state lifetimes. After an optical pump pulse, a resonant microwave  $\pi$ -pulse is applied to exchange the populations of selected spin sublevels and thereby control the dominant decay constants, **b**, Decay curves of the shelving state population described by double exponential functions  $y = c - a_1 \exp(-t/\tau_1) - a_2 \exp(-t/\tau_2)$ . Blue: experimental data, red dashes: double exponential fits (see SI). For each panel, the microwave  $\pi$ -pulse is resonant with the denoted ESR transition, **c**, Assignment of the decay constants to the triplet energy levels. The initial populations (no ESR), are proportional to the decay constants. The small population of the short lived state is omitted. The observed decay constants imply the assignment of the energy levels denoted on the left, **d**, Summary of the triplet kinetics and electronic structure consisting of singlet ground- and excited states and a meta-stable triplet state. Transition rates between two states  $i$  and  $j$  and the lifetime of a state  $i$

are denoted  $\gamma_{ij}$  and  $\tau_i$ , respectively.

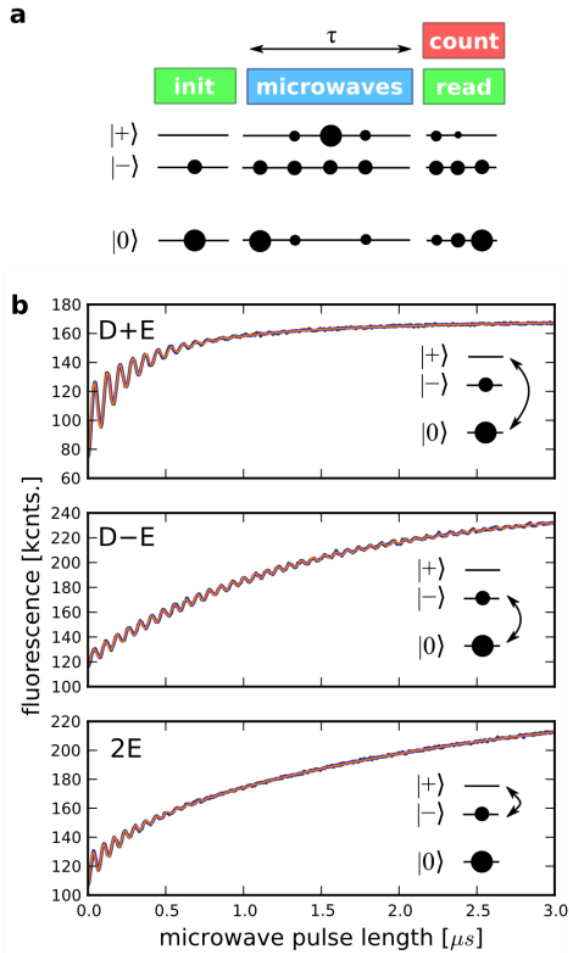


**Fig. 4 | Coherent triplet spin manipulation.** **a**, Optical and microwave pulse sequence and evolution of the triplet populations (here illustrated for microwaves resonant with the D+E transition), **b**, Rabi oscillations among the triplet spin sublevels. Thick blue lines show experimental data, thin red lines show theoretical fits with the model  $I = I_0 - a_1 + a_2 \cos \Omega t \exp -t/\tau - a_3 \exp(t/\tau)$ , where  $\tau = 2(\tau_\alpha^{-1} + \tau_\beta^{-1})^{-1}$  is a combined decay constant of the levels  $\alpha$  and  $\beta$  involved in the Rabi oscillations,  $\tau$  is the decay constant of the remaining level,  $a_i$  are fluorescence amplitudes and  $\Omega$  is the Rabi frequency. Note that for the upper and lower panel the combined decay constant is dominated by the fast decay of the  $|+\rangle$  level. For the fit shown in the middle panel the last term is omitted, since the unaffected level is the  $|+\rangle$  level, which (nearly) unpopulated.

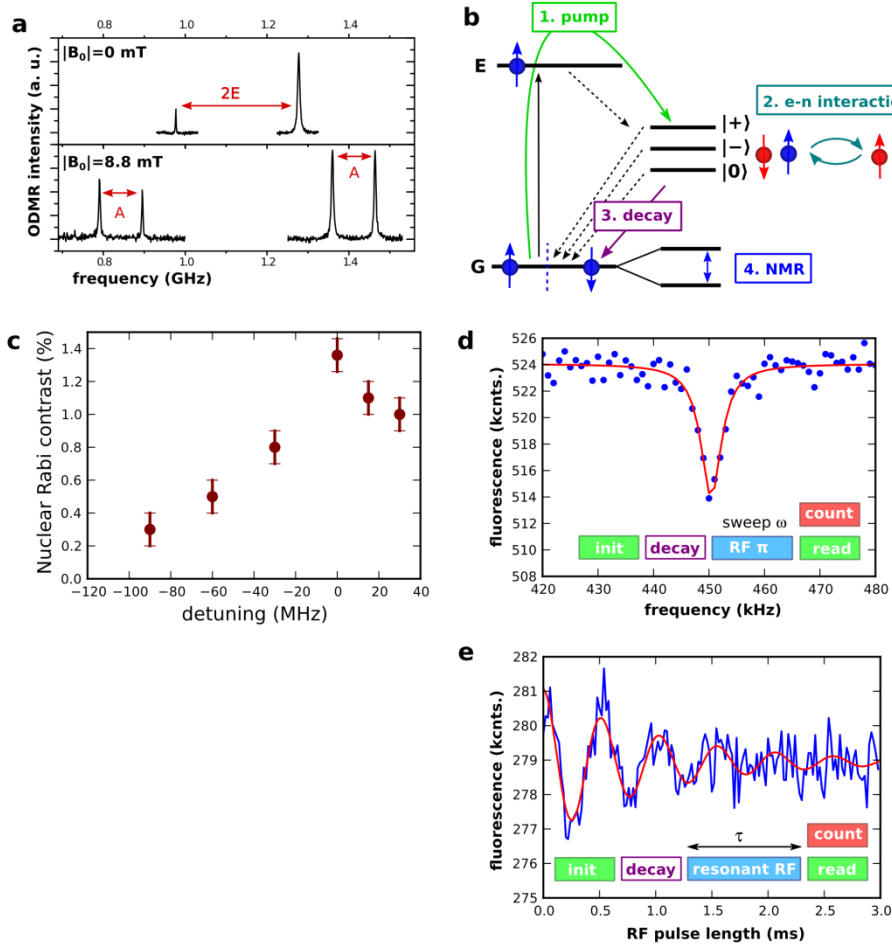


**Fig. 5 | Readout and control of a single nuclear spin in the spin-free electronic ground state.** **a**, ODMR spectra of an ST1 defect with a nearby  $^{13}\text{C}$  nuclear spin, under zero (upper panel) and moderate (lower panel) magnetic field applied along the defect's axis. E and A denote the zero-field- and hyperfine-splitting parameters, respectively. The hyperfine splitting is suppressed at small fields and becomes visible when the Zeeman energy is larger than the E parameter. **b**, Readout and control of the nuclear spin with the electronic triplet spin ancilla. The nuclear spin (blue arrows) is interrogated by optically pumping the electron spin (red arrows) into the triplet state and allowing the electron and nuclear spin to interact. The subsequent decay of the triplet state destroys the electron spin and leaves the nuclear spin unchanged. The bare nuclear spin is then coherently manipulated by NMR. Efficient transfer of spin polarization between the electron and nuclear spin in the triplet state is provided by exploiting an ONP as a consequence of LAC between the  $| -1, +1/2 \rangle$  and  $| 0, -1/2 \rangle$  hyperfine levels (see text), **c**, Signal contrast of nuclear Rabi oscillations, corresponding to the product of the nuclear spin polarization and readout contrast, as a function of detuning from the LAC (zero detuning corresponds to the LAC). **d,e**, NMR spectrum and Rabi oscillations of the nuclear spin in the electronic ground state. For the NMR spectrum (d), an RF  $\pi$ -pulse of variable frequency is inserted between the preparation and readout laser pulses. The resonance dip corresponds to the Larmor precession of a bare  $^{13}\text{C}$  nuclear spin. Blue: experimental data, Red: Lorentzian fit. For the Rabi oscillations (e) a resonant RF pulse of variable length

is inserted between the initialization and readout laser pulses. Blue: experimental data, red: exponentially decaying cosine fit; decay constant 1.0(1) ms.

# Readout and control of a single nuclear spin with a meta-stable electron spin ancilla

—

## Supplementary information

S.-Y. Lee, M. Widmann, T. Rendler, M. Doherty, T. Babinec, S. Yang,  
M. Eyer, P. Siyushev, B. Haussmann, M. Loncar, Z. Bodrog,  
A. Gali, N. Manson, H. Fedder, J. Wrachtrup

October 29, 2018

### 1 Introduction

Here we present supporting material to the key results and arguments found in the main text. In particular, we analyze the properties of the ST1 defect that we observed through our employment of various optical spectroscopy and magnetic resonance techniques. From our analysis, we draw key conclusions about the structure of the ST1 defect and its electronic levels. These conclusions will provide the foundations for future studies of the formation of the ST1 defect and its properties. Our methodology draws many parallels with the vital early investigations of the NV center [1, 2, 3, 4, 5, 6, 7]. Further, we consider the mechanisms underlying optical nuclear spin-polarization, -readout and -decoherence in greater detail. Here we draw on early works on optical nuclear polarization [8, 9] and  $^{13}\text{C}$  relaxation in diamond [10, 11].

### 2 Sample fabrication and the occurrence of ST1 defects

Arrays of diamond nano wires (length 2  $\mu\text{m}$ , diameter 200 nm, pitch 2  $\mu\text{m}$ ) were fabricated into the cleaved [111] surface of an HPHT diamond (element six Ltd.) by reactive ion etching as described in detail in [12]. In brief: first, an HSQ mask is defined with e-beam lithography and a lift-off process. Thereafter, anisotropic etching is performed with an inductively coupled oxygen plasma. After the nano wire fabrication, the sample is annealed in vacuum at 850  $^{\circ}\text{C}$  for several hours and subsequently boiled in a mixture of equal amounts of perchloric-, sulfuric-, and nitric acid at 100  $^{\circ}\text{C}$ . 32 arrays, each containing 8080 nano wires were fabricated and the ST1 defects were found in all patches that were investigated. A randomly chosen area (100 $\mu\text{m}$ 100 $\mu\text{m}$ ) on one of the patches was intensively investigated in a home built confocal fluorescence microscope (Nikon LU Plan Fluor Epi 100x, 0.9 N.A. air objective, 532 nm laser excitation) and 19 single ST1 defects were found within this area. This number is equivalent to approximately one ST1 defect per 800 nano-wires. Note that the number of NV defects in this area is considerably smaller than the number of ST1 defects (only about 5) and agrees roughly with the amount expected from the bulk NV- concentration. All ST1 defect fluorescence was observed on nano-wires. The bulk diamond underneath and the surface next to the wires was carefully investigated by fluorescence microscopy and no ST1 defects were observed. Note that this fact might be biased by the positive role of the nano-wires on the optical collection efficiency [13]. Due to the high collection efficiency of the nano wires, ST1 defects in the bulk would appear a factor of about 5 times dimmer than the defects on the nano-wires. This might render them hardly visible against the background fluorescence, which is about 10 kcnts./s on the plane sample surface and about 100 kcnts./s on an empty wire the present case. Since the nano-wires have a tendency to attract fluorescent material from the environment whose

emission then couples efficiently into the wires and produces background fluorescence, during the past, the sample surface had been cleaned several times by slowly scanning the laser over the surface (incident power  $\sim 10$  mW). This procedure bleaches most of the adsorbed molecules and removes most of the background fluorescence. At present we cannot exclude that this strong laser illumination in combination with ambient adsorbates plays a role for the occurrence of the ST1 defects. Thus, we can identify three aspects that might contribute to the occurrence of ST1 defects.

- The [111] crystal surface
- The fabrication process, in particular the plasma etching using oxygen gas (trace amounts of contaminants from the chamber and electrodes may also play a role) and subsequent annealing
- Adsorbate molecules in combination with strong 532 nm laser illumination

As we will discuss below, oxygen is a possible defect constituent since it does not have a nuclear spin and is capable of  $sp^3$  bonding. Future oxygen implantation and reactive ion etching studies can be used to probe this hypothesis. Recently a defect with a ZPL at 547.2 nm has been reported in HPHT diamonds grown with a Ni-containing catalyst at elevated temperatures ( $>1400$  °C); PL spectra measured under 337.1 nm excitation [14]. We think that the difference of the observed ZPL compared to the ZPL observed in the present work at 550(1) nm is too large to identify both defects as the same species. Nevertheless, a shift of a ZPL e.g. due to lattice deformations or co-presence of another impurity species might still be possible. More importantly, for the 547.2 nm defect, an excited state lifetime of 150 s was reported which differs substantially from the excited state lifetime of the ST1 defect of about 10 ns. Our current working hypothesis is that the defect observed in the present work is a different one.

### 3 Properties of the optical fluorescence

Under 532 nm excitation, the fluorescence of the ST1 defect exhibits a zero phonon line (ZPL) at 550 nm (2.25 eV) and a broad vibronic band that extends to lower energy  $\sim 750$  nm (refer to figure S1). The association of this fluorescence with the ST1 defect (and not with some other unidentified emission states in the nano-wires) was established by two different methods. Firstly, in order to verify that this emission is responsible for the observed single photon emission, the second order correlation measurement was repeated in the presence of a band pass filter centered at 550 nm (band width 25 nm) and identical anti-bunching behavior was observed. In order to confirm that ESR gives rise to the enhancement of this emission, the PL spectra were measured while applying on- and off-resonant microwave excitation. Figure S1 shows that both the ZPL and its phonon side band were enhanced when the on-resonance microwave was applied. Note that the PL without MW was identical to PL with off-resonance MW (not shown).

The energy of the fluorescence and the existence of the sharp ZPL implies that the electronic transition occurs between energetically discrete electron orbitals within the diamond bandgap (refer to figure S2) [15]. As the shape of the vibronic band in the PL spectra of figure S1 is distorted by the first and second order Raman resonances of the 532 nm excitation, it is not possible to directly establish the Huang-Rhys factor of the fluorescence. The Huang-Rhys factor describes the relative intensity of the ZPL and the vibronic band and is a measure of the lattice relaxation associated with the electronic transition [15]. Since the Raman resonances should not change in the presence of microwaves, the difference in the PL spectra while applying on- and off-resonance microwaves provides a reasonable picture of the ZPL and vibronic band that is free of distortions from the Raman resonances. It is apparent that like many other color centers in diamond, the Huang-Rhys factor at room temperature is appreciable (estimate at least greater than one) and that there is an appreciable lattice relaxation associated with the electronic transition [1, 16]. The difference between the first moment of the vibronic band and the ZPL energy is  $\sim 0.15$  eV at room temperature, which provides an estimate of the Anti-Stokes shift and lattice relaxation energy associated with the transition [15]. Further studies of the vibronic band will provide additional information on the electron-phonon interactions of the ST1 defect [17].

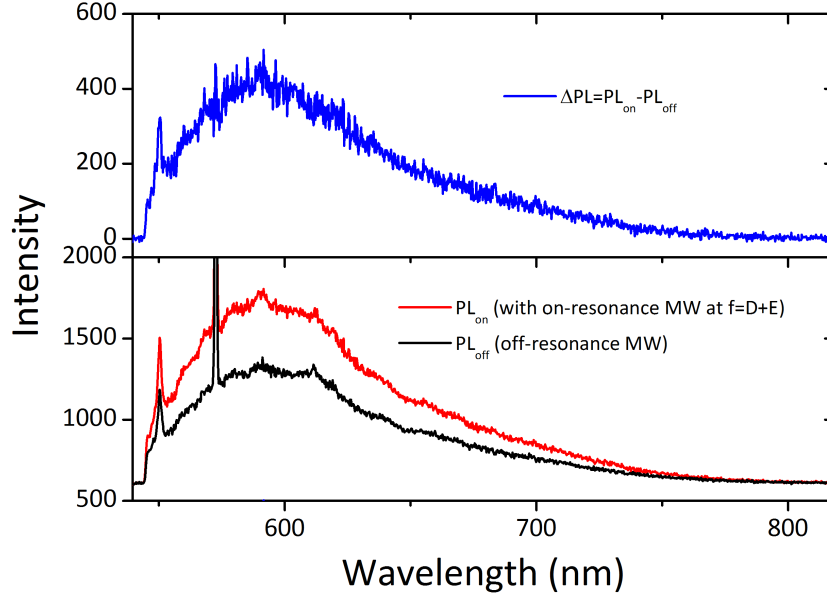


Figure S1: **Enhancement of emission induced by ESR.** Low panel: Two PL spectra measured at room temperature with on- and off-resonance continuous ESR excitation. Upper panel: Difference between two spectra. Enhancement of both ZPL and phonon side band can be seen. The sharp peak at 573 nm is the Raman peak.

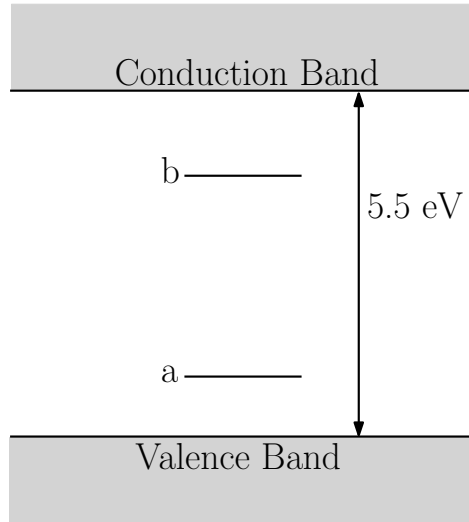


Figure S2: **Electron orbitals of the ST1 defect.** The shaded regions represent the diamond valence and conduction bands separated by the indirect bandgap of  $\sim 5.5$  eV. The solid lines within the band gap represent the energies of the orbitals of the ST1 defect that are involved in the optical transition. The  $a$  orbital is the highest occupied orbital in the electronic ground state. Optical excitation results in the promotion of an electron from the  $a$  orbital to the lowest unoccupied orbital  $b$ . The symmetries of the orbitals are unknown. There may exist other orbitals of the ST1 defect in the bandgap.

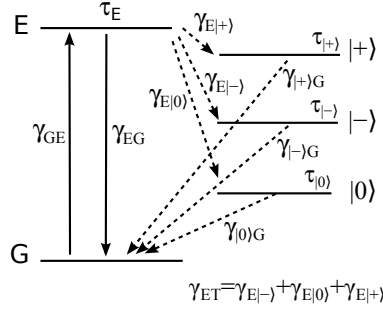


Figure S3: **Rate equation model.** The ground and excited states are denoted  $G$  and  $E$ . The three triplet spin levels are denoted  $|0\rangle$ ,  $|-\rangle$  and  $|+\rangle$ . Rates and lifetimes are denoted by greek letters  $\gamma$  and  $\tau$ , respectively.

## 4 Electronic structure and optical cycle

It was discussed in the main text that the key experimental observations that suggest the existence of a metastable triplet state are the *increase of the fluorescence* under application of a strong misaligned magnetic field or resonant microwave field, and *pronounced photon bunching* under saturated optical excitation (refer to Fig. 1, main text). Such behaviour is well known for fluorescent molecules with singlet ground and excited states and a long lived excited triplet state that features different lifetimes of the individual triplet spin sublevels [18]. The triplet state plays the role of a shelving state. When the population is cycled between the ground and excited state by optical pumping, part of the population gets trapped in the triplet state. This Inter-System-Crossing (ISC) leads to an overall reduced fluorescence since the ISC transitions are typically non-radiative and the lifetime of the triplet state is long (ISC transitions are only weakly allowed by spin-orbit or spin-spin interaction). The long lifetime leads to characteristic 'bunching shoulders' in the second order photon correlation. When either the population- or the decay rates of the triplet sublevels are different, the sublevels are not equally populated, i.e., the spin becomes polarized. Spin polarization is typically built up during several optical pump cycles. When the decay rates of the triplet sublevels are different, a mixing of the triplet populations (either by a resonant microwave field or by a strong misaligned magnetic field), results in a faster or slower deshelling of the triplet state. This leads to an increase or decrease of the emission intensity.

In the following, we analyze the optical cycle and provide conclusions about the defect electronic structure. We first present a 5-level rate equation model to describe the optical cycle. Thereafter we experimentally determine the transition rates. Finally we draw conclusions for the electronic structure and symmetry of the electronic states.

### 4.1 Rate equation model

The rate equation model is illustrated schematically in figure S3. It consists of five levels: the ground and excited states  $G$  and  $E$  and the three triplet spin levels  $|0\rangle$ ,  $|-\rangle$  and  $|+\rangle$ . Rates between levels  $\mu$  and  $\nu$  are denoted by  $\gamma_{\mu\nu}$  and the lifetime of a level  $\mu$  is denoted by  $\tau_{\mu}$ .  $\gamma_{GE}$  is the optical pump rate,  $\gamma_{EG}$  is the spontaneous emission rate,  $\gamma_{E\nu}$ ,  $\nu = |0\rangle, |-\rangle, |+\rangle$  are the triplet population rates and  $\gamma_{G\nu}$ ,  $\nu = |0\rangle, |-\rangle, |+\rangle$  are the triplet decay rates. The rates are related to the lifetimes  $\tau = 1/\sum \gamma_{\nu}$ . The time evolution of the

populations  $n = (n_G, n_E, n_{|+\rangle}, n_{|-\rangle}, n_{|0\rangle})$  is given by the rate equations

$$\begin{aligned}
\dot{n}_G &= -\gamma_{GE}n_G + \gamma_{EG}n_E + \gamma_{|+\rangle G}n_{|+\rangle} + \gamma_{|-\rangle G}n_{|-\rangle} + \gamma_{|0\rangle G}n_{|0\rangle} \\
\dot{n}_E &= +\gamma_{GE}n_G - \gamma_{EG}n_E - (\gamma_{E|+\rangle} + \gamma_{E|-\rangle} + \gamma_{E|0\rangle})n_E \\
\dot{n}_{|+\rangle} &= +\gamma_{E|+\rangle}n_E - \gamma_{|+\rangle G}n_{|+\rangle} \\
\dot{n}_{|-\rangle} &= +\gamma_{E|-\rangle}n_E - \gamma_{|-\rangle G}n_{|-\rangle} \\
\dot{n}_{|0\rangle} &= +\gamma_{E|0\rangle}n_E - \gamma_{|0\rangle G}n_{|0\rangle}
\end{aligned} \tag{S.1}$$

Using the conservation of the total population

$$1 = n_G + n_E + n_{|+\rangle} + n_{|-\rangle} + n_{|0\rangle}, \tag{S.2}$$

one equation and one variable in Eq.(S.1) can be eliminated. The result is a regular first order linear differential equation with constant coefficient matrix  $A$  and right hand side vector  $b$ .

$$\dot{n} = An + b, \tag{S.3}$$

which has the solution

$$n(t) = e^{At}n_0 + A^{-1}e^{At}b - A^{-1}b, \tag{S.4}$$

where  $n_0$  are the initial populations. Using such a model, all photophysical properties, such as the saturation behavior, anti-bunching, fluorescence response to an optical pump pulse, etc., can be easily computed numerically by diagonalizing the coefficient matrix  $A$  or in some cases analytically. In the following sections, we will experimentally determine the decay rates  $\gamma_{|+\rangle G}, \gamma_{|-\rangle G}, \gamma_{|0\rangle G}$  and the total population rate  $\gamma_{ET} = \gamma_{E|+\rangle} + \gamma_{E|-\rangle} + \gamma_{E|0\rangle}$  of the triplet level, where we assume that the population rates of the triplet state are faster than the decay rates and are equal for all spin sublevels, and the triplet decay rates are distinct. In this case, the populations of the triplet levels under saturated optical excitation are proportional to their lifetimes.

## 4.2 Triplet lifetimes

As discussed in the main text, in order to determine the triplet decay rates, the recovery of the ground state population was observed by a pulsed optical experiment (refer to Fig.3, main text and figure S4). First a long laser pulse is applied (duration longer than the triplet lifetimes, power high enough to saturate the optical transition). At the end of the pulse the system is in the steady state under saturated optical illumination, i.e., the triplet levels are maximally populated. The relative populations of the sublevels are proportional to their lifetimes. Next, the triplet levels are allowed to decay for a variable amount of time in the range few ns to several s. Finally, the population of the ground state is measured by applying a second laser pulse that is identical to the first pulse and simultaneously recording the fluorescence. The integrated fluorescence is proportional to the ground state population before the pulse. Most data was accumulated until the standard deviation of the measured ground state populations (given by photon shot noise) was below 1%. Exponentially increasing fluorescence curves were obtained. The time constants are given by the lifetimes of the triplet sublevels. The data was fit with single-, double- and triple-exponential models and the goodness-of-fit  $Q = \Gamma(0.5\nu, 0.5\chi_0^2)$  was evaluated for each fit [19]. Here  $\Gamma$  is the complementary incomplete gamma function,  $\nu$  is the degrees of freedom and  $\chi_0^2$  is the  $\chi^2$  evaluated at the minimum. Single exponential fits typically result in goodness of fit values  $Q < 10^{-10}$  and can be discarded. Most Double- and triple-exponential fits result in goodness-of-fit values in the range  $1 < Q < 10^{-3}$  and are both acceptable. The triple-exponential models typically contain one component whose amplitude is much smaller than the two other components and therefore this component can be safely neglected. This reflects the fact that acceptable goodness-of-fit values are readily obtained with double exponential fits. We conclude that double exponential fits are faithful models for all data. To assign the lifetimes to the spin sublevels, we perform the measurement with an additional microwave  $\pi$ -pulse inserted after the optical pump pulse. The microwave power is high enough, such that the duration of the microwave pulse is short compared to the lifetimes. The

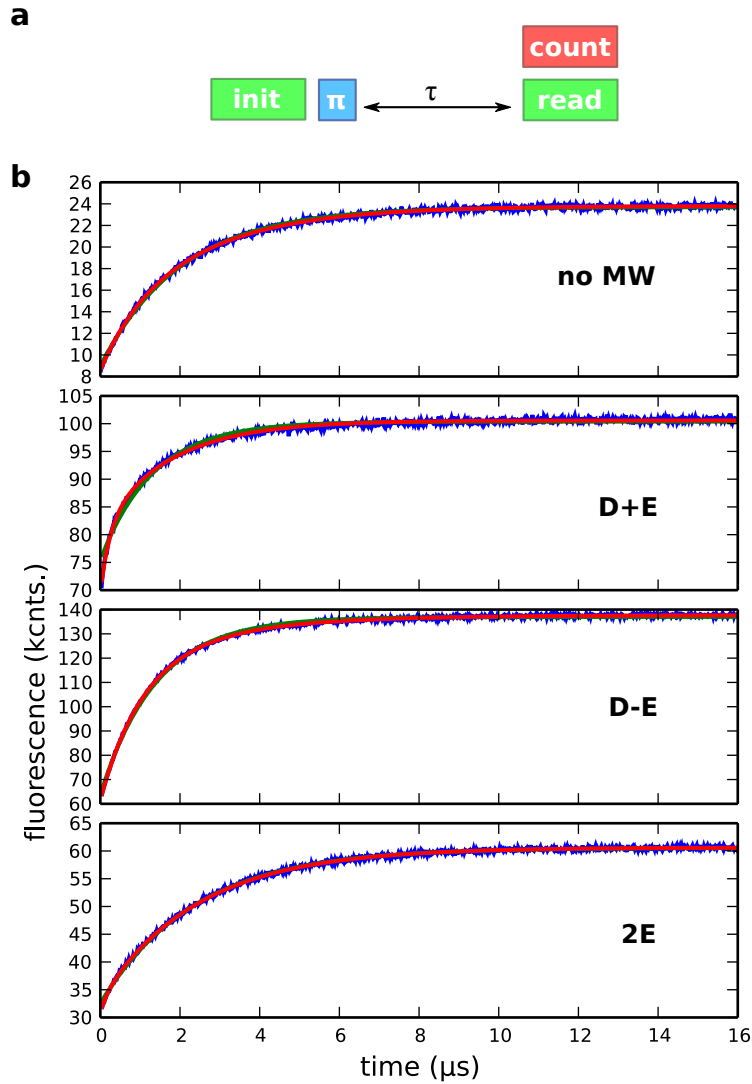


Figure S4: **Experimental determination of the Triplet lifetimes.** **a**, Pulse sequence. **b**, Measured decay curves for defect C (see text), without microwave pulse and with a  $\pi$ -pulse tuned in resonance with the three ESR transitions. Blue dots: experimental data, solid green lines: single exponential fits, solid red lines: double exponential fits.

ST1	no MW	D+E	D-E	2E
A	930(37)	161(5)	775(39)	158(19)
	2288(21)	1029(13)	2358(32)	2448(13)
	11054(700)	37492(695)	8212(515)	1249(20)
	41878(720)	44867(672)	22750(532)	11988(40)
	4.7e-2	3.3e-2	4.2e-2	6.0e-2
B	761(52)	267(7)	865(9)	239(32)
	2329(35)	1641(24)	2908(74)	2390(9)
	3630(316)	23878(340)	60634(694)	2068(136)
	13419(323)	20388(336)	19072(712)	32700(93)
	4e-5	2e-32	7e-5	2.6e-3
C	936(74)	247(9)	1055(15)	181(20)
	2473(56)	1757(17)	2812(99)	2447(9)
	3838(493)	11730(216)	56834(1256)	2444(147)
	11396(499)	19118(194)	19265(1272)	27342(69)
	2.3e-3	1.5e-13	1.3e-3	2.2e-2
summary	1000	200	1000	200
	2500	1000	2500	2500

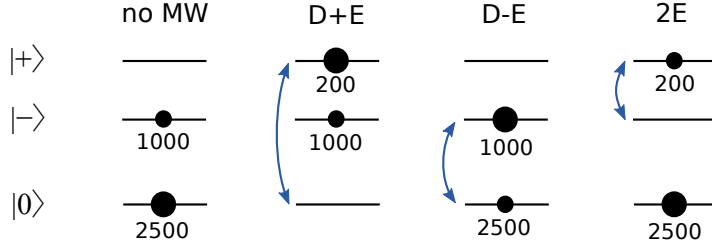


Table S1: **Measured triplet lifetimes of three ST1 defects A,B,C.** The data in each cell shows (from top to bottom) the two time constants [ns], the two amplitudes [counts] and the goodness-of-fit of a double exponential model. The last row summarizes the observed time constants [ns]. The mean and standard deviation over equivalent time constants yields  $\tau_{|0\rangle} = 2500(204)$  ns,  $\tau_{|-\rangle} = 1072(350)$  ns,  $\tau_{|+\rangle} = 209(44)$  ns

microwave frequency is tuned in resonance with each of the triplet spin transitions. The microwave  $\pi$ -pulse swaps the population of the triplet sublevels and thereby exchanges the amplitudes of the corresponding exponential decay curves. Table S1 summarizes the measured decay constants and amplitudes and specifies the goodness-of-fit values for three different ST1 defects. Importantly, there are only minor deviations among the different defects. Generally three distinct time constants are observed, of about 200 ns, 1000 ns and 2500 ns. The result is summarized in the last row. The result is used to assign the time constants to the spin levels as shown in the illustration below the table. To obtain an overall average for the decay constants, we evaluate the mean and standard deviation over all equivalent time constants, yielding  $\tau_{|0\rangle} = 2500(204)$  ns,  $\tau_{|-\rangle} = 1072(350)$  ns,  $\tau_{|+\rangle} = 209(44)$  ns.

### 4.3 Triplet population rates

In the following, we determine the triplet population rates by two different methods. One approach exploits the second order correlations,  $g^{(2)}$ , of the photon emission at different excitation powers. The numerical solutions is fit based on the five level rate model described in equation (S.1) yielding the population rate parameters. The measured  $g^{(2)}$  functions and fitting results are shown in figure S5. Two representative

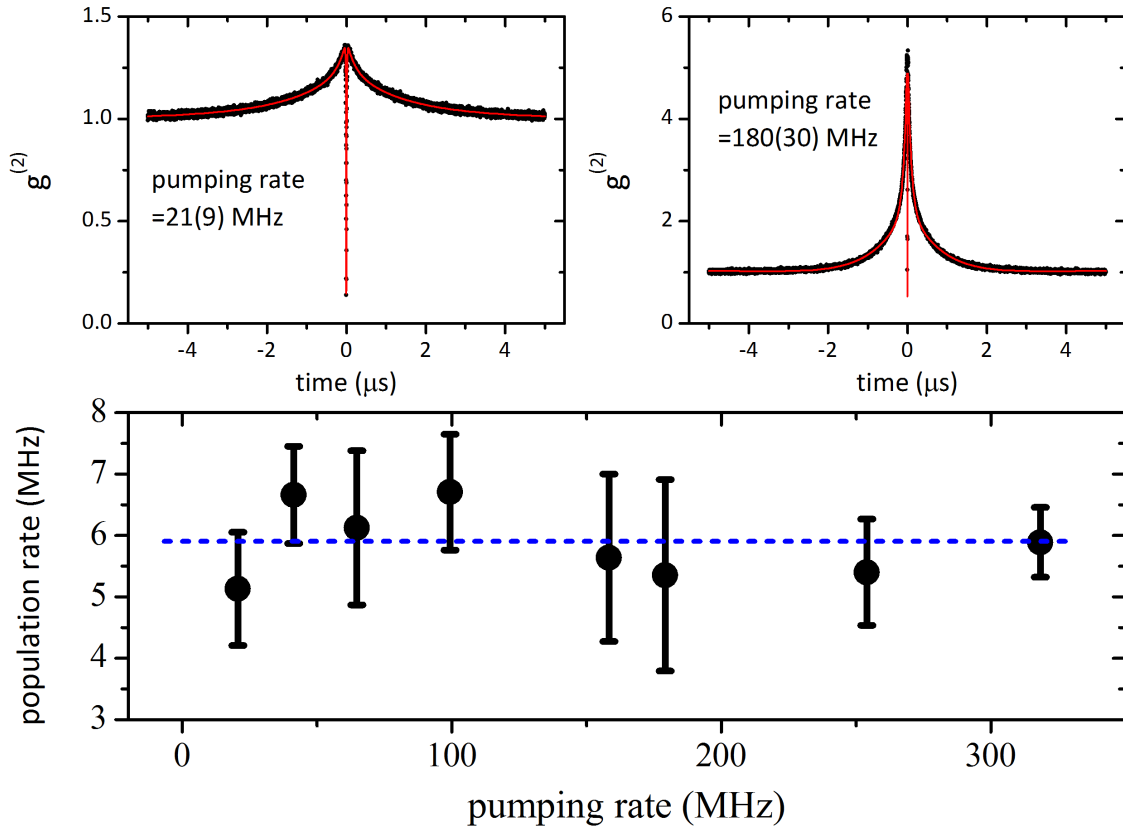


Figure S5: **Determination of the population Rates.** Two upper panel: measured  $g^{(2)}$  functions at low and high optical excitation powers. Red lines are the fitted curves. Instead of the excitation powers, the extracted pumping rates are shown. Lower panel: The obtained population rates as a function of the pumping rate. Only a common value 5.9(6) MHz was obtained because the three population rates could not be distinguished. Blue dotted line indicates this value which is almost constant.

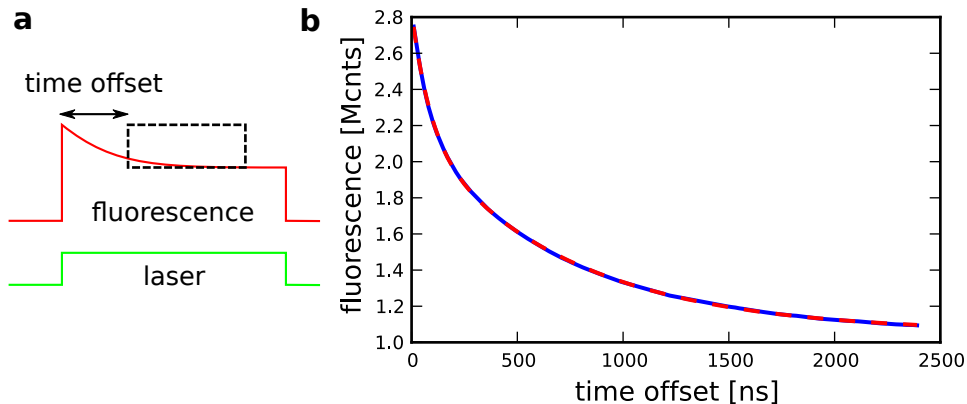


Figure S6: **Determination of the overall triplet population rate by pulsed optical excitation.** a) Schematic of the measurement and data analysis. The stimulation consists of optical pulses that are separated by idle times. Both are longer than the triplet lifetimes. The resulting fluorescence response profile is processed by integrating the fluorescence over a window of fixed length and moving this window over the profile, starting from the initial rising edge. b) Experimental data (blue solid line) and double exponential fit (red dashed line), providing two time constants  $\tau_1 = 85\text{ns}$  and  $\tau_2 = 724\text{ns}$ .

$g^{(2)}$  functions measured at low and high excitations are shown. Both the anti-bunching part and bunching shoulder can be well identified. Since the excited singlet state life time and the triplet state life times are already known, the measured  $g^{(2)}$  functions can be fitted with four free parameters, namely the pump rate and the three population rates. Three population rates, however, could not be distinguished within the error range, instead the fit was simplified to two free parameters by considering the total rate  $\gamma_{ET} = (56(7)\text{ ns})^{-1}$ , where we assume  $\gamma_{E|+} = \gamma_{E|-} = \gamma_{E|0}$ . Note that whilst ISC selection rules likely imply that the populations rates could differ, such differences will not significantly effect the application of the rate model in the present section.

A second method for determining the triplet population rates is to use a pulsed optical experiment. We expect that the population rates of the triplet sublevels are similar for all three levels and the time scales of population and decay are well separated (the population rates and decay rates differ by about an order of magnitude). If this was not the case, we would expect a more complicated decay behavior in the lifetime measurements. In this case, the total transition rate from the excited state to the triplet levels can be determined from the fluorescence response of the system to a single optical pulse as shown in Fig.S6a. The length of the laser pulses and the idle time between two pulses is much longer than the triplet lifetime. If the laser is set to high power such that the optical transitions is saturated, the ground state is essentially depleted and first all population resides in the excited state. The population then starts to leak to the triplet state. Thus, the length of the excitation pulse determines how much population is transferred. Since the lifetimes of the triplet state are much longer than the population rates, recycling of population through the triplet and ground state during this process is negligible. Therefore, an approximate exponential increase of the triplet population is expected with time constant  $\tau_{ET} = \gamma_{ET}^{-1}$ . As before, the triplet population can be measured by a readout laser pulse and recording the fluorescence response profile. In the present measurement, the initialization and readout laser pulses can be merged to a single pulse and the distinction between the two pulses is achieved by moving the integration window for the determination of the triplet population over the pulse profile (refer to figure S6a). The result of this measurement is shown in Figure S6b. A double exponential decay is observed. The short time constant reflects the buildup of the triplet population. The longer time constant reflects the time required to reach the steady state under optical pumping and is given by a combination of the different decay rates. The combined population rate is found from the short time constant as  $\gamma_{ET} \approx (85\text{ ns})^{-1}$ . This value agrees reasonably well with the value of about 56 ns obtained from the photon auto-correlation. Appreciating both independent methods, we estimate  $\gamma_{ET} \approx (70(20)\text{ ns})^{-1}$ .

#### 4.4 Application of the rate equation model

In this section we provide further detail about the rate equation model. In particular, we present that the recovery of the ground state population as observed in Fig 3 in the main text is the evidence for the triplet meta stable state and analyze how the observed amplitudes of exponentially decaying components of the triplet levels are related to the rate parameters. To this end, the analytical solutions for the ground state spin recovery without and with  $\pi$ -pulses will be introduced. The steady state solutions based on the rate model can be easily found (not shown) and can be considered as initial values at  $t = 0$  for the ground state recovery measurement. Then the spin populations of each states after time  $\tau'$  (while  $\gamma_{GE} = 0$ ) can be found. In the experiments, a 6 s long readout pulse was applied at  $t = \tau'$  and the fluorescence response was integrated only over a short (20 ~ 200 ns) period at the very beginning of the readout window. Because no significant difference in the integrated signal was found up to a 200 ns long integration window, we suppose that the repolarization hardly affected so that the integrated intensity is directly proportional to the ground state spin population after  $\tau'$ . Thus the ground state spin population at  $t = \tau'$  is only of our interest, which is

$$n_G(\tau') = C_1 \cdot n_G(0) \cdot e^{-\Gamma \cdot \tau'} - \sum_{i=|+\rangle, |-\rangle, |0\rangle} \frac{\Gamma}{\Gamma - \gamma_{iG}} \cdot n_i(0) \cdot e^{-\gamma_{iG} \cdot \tau'} + C_0 \cdot n_G(0) \quad (\text{S.5})$$

where  $n_i(0)$  is the initial value for each state which is equivalent to the steady state value,  $\Gamma = \gamma_{EG} + \gamma_{E|+\rangle} + \gamma_{E|-\rangle} + \gamma_{E|0\rangle}$ ,  $C_1 = -\frac{\gamma_{EG} \cdot \gamma_{GE}}{\Gamma^2} + \sum_{i=|+\rangle, |-\rangle, |0\rangle} \frac{\gamma_{iG} \cdot \gamma_{Ei} \cdot \gamma_{GE}}{\Gamma^2 \cdot (\Gamma - \gamma_{iG})}$ , and  $C_0 = 1 - C_1 + \sum_{i=|+\rangle, |-\rangle, |0\rangle} \frac{\gamma_{Ei} \cdot \gamma_{GE}}{\gamma_{iG} \cdot (\gamma_{EG} - \gamma_{iG})}$ . When an ideal resonant  $\pi$ -pulse between two sublevels,  $|+\rangle$  and  $|-\rangle$  for instance, is applied right after the initialization pulse, the initial population of these two states are exchanged. The solution for this case becomes

$$n_{G,|+\rangle|-\rangle}(\tau') = C_1 \cdot n_G(0) \cdot e^{-\Gamma \cdot \tau'} - \sum_{i,j=|+\rangle, |-\rangle, i \neq j} (n_j(0) + \frac{\gamma_{iG}}{\Gamma - \gamma_{iG}} \cdot n_i(0)) \cdot e^{-\gamma_{iG} \cdot \tau'} - \frac{\Gamma}{\Gamma - \gamma_{|0\rangle G}} \cdot n_{|0\rangle}(0) \cdot e^{-\gamma_{|0\rangle G} \cdot \tau'} + C_{0,|+\rangle|-\rangle} \cdot n_G(0) \quad (\text{S.6})$$

where  $C_{0,|+\rangle|-\rangle}$  is a constant similar with  $C_0$ . Solutions for the two other cases  $n_{G,|+\rangle|0\rangle}(\tau')$  and  $n_{G,|-\rangle|0\rangle}(\tau')$  also can be found (not shown). Both solutions consist of four exponential terms, but the first term has little contribution because its decay is faster than the others ( $\Gamma > \gamma_{EG} \gg \gamma_{iG}$ ) by at least one order of magnitude, and its amplitude is very small too as will be seen later. In addition, because the found triplet state life times are at least one order of magnitude slower than the excited singlet state life time, we get  $\gamma_{iG}/(\Gamma - \gamma_{iG}) \ll 1$  and  $\Gamma/(\Gamma - \gamma_{iG}) \approx 1$ . Thus the above solutions can be rewritten as

$$n_G(\tau') \approx - \sum_{i=|+\rangle, |-\rangle, |0\rangle} n_i(0) \cdot e^{-\gamma_{iG} \cdot \tau'} + C_0 \cdot n_G(0), \quad (\text{S.7})$$

$$n_{G,|+\rangle|-\rangle}(\tau') \approx - \sum_{i,j=|+\rangle, |-\rangle, i \neq j} n_j(0) \cdot e^{-\gamma_{iG} \cdot \tau'} - n_{|0\rangle}(0) \cdot e^{-\gamma_{|0\rangle G} \cdot \tau'} + C_{0,|+\rangle|-\rangle} \cdot n_G(0). \quad (\text{S.8})$$

Thus one can conclude that the observed ground state recovery curve can be explained well by three exponential decay terms of which decay constants are the decay constants of the triplet sublevels or even the double exponential decay if one of the three decay terms is too small. And the inserted  $\pi$ -pulse does not alter the decay constants but only exchanges the amplitudes of the sublevels under the influence of the applied  $\pi$ -pulse as long as the excited singlet state life time is faster than the triplet state life times. Therefore, one can assign the measured decay constants to each sublevels by comparing the amplitudes of each decay terms obtained with and without applying  $\pi$ -pulses. In order to make an indisputable conclusion, it is better to compare the numerically simulated amplitudes of each decaying components with the observed ones.

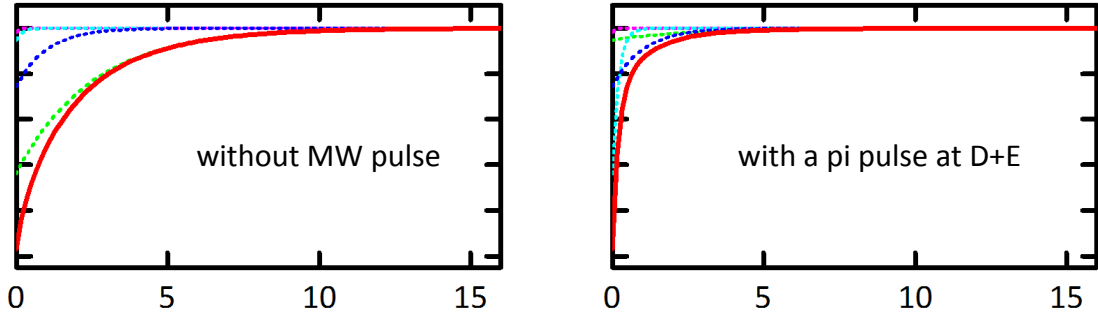


Figure S7: **Numerical simulations of the ground state recovery measurements.** Red lines are the simulated recovery curves, cyan, blue, and green curves are the exponential decays of  $|+\rangle$ ,  $|-\rangle$ , and  $|0\rangle$ , respectively. The first exponential terms (violet lines) in equation (S.5) and (S.6) are almost ignorable because of their fast decay and small amplitudes.

The numerical simulations using the exact solution, equations (S.5) and (S.6) with the set of parameters of  $\gamma_{EG} = (10 \text{ ns})^{-1}$ ,  $\gamma_{GE} = (10 \text{ ns})^{-1}$ ,  $\gamma_{E|+} = \gamma_{E|-} = \gamma_{E|0} = (170 \text{ ns})^{-1}$ ,  $\gamma_{|+ \rangle G} = (200 \text{ ns})^{-1}$ ,  $\gamma_{|- \rangle G} = (1000 \text{ ns})^{-1}$ ,  $\gamma_{|0 \rangle G} = (2500 \text{ ns})^{-1}$  are shown in figure S7. Note that the common value of 170 ns was used for three population rates and the typical value for the optical pumping rate  $\gamma_{GE} = (10 \text{ ns})^{-1}$  was used. The first term in equations (S.5) and (S.6) (violet curves in figure S7) of which decay constant is  $\Gamma = \gamma_{EG} + \gamma_{E|+} + \gamma_{E|-} + \gamma_{E|0}$ , is negligible because it decays very quickly and the amplitude is minute. Among the remaining three exponential decays originated from the decays of the triplet sublevels, the amplitude of the fastest decay is smaller than others, so this decay is hardly detectable in measured data as already shown above. Overall, these simulated curves are in close agreement with the measured ones and can explain the measured curves very well. The simulated and measured amplitudes of each decay terms are summarized in table S2. The measured amplitudes without applying  $\pi$ -pulses are in very good agreement with the simulations. The exchange of the initial populations by the coherent  $\pi$ -pulses are well described in both measured and simulated values, and they are in good agreement. The found discrepancy between the size of the simulated and the measured amplitudes can have a few origins: intersystem crossing among each sublevels, non-ideal  $\pi$ -pulses.

	simulated			measured		
	A+	A-	A0	A+	A-	A0
without MW	0.2	1.0	2.4	-	1.0(1)	2.3(1)
D+E	2.4	1.0	0.2	1.11(4)	1.00(3)	-
D-E	0.2	2.4	1.0	-	1.7(1)	1.0(1)
2E	1.0	0.2	2.4	1.00(9)	-	10.16(4)

Table S2: **Comparison of the measured amplitudes with the simulations.** The observed switching of the initial populations by  $\pi$ -pulses are in consistent with the simulations.

#### 4.5 Conclusions for the electronic structure

As discussed in the previous sections, the observed behaviour of the optical fluorescence implies that the optically detected magnetic resonance occurs within a metastable spin triplet level that exists energetically between the ground and optically excited levels of the defect. It was also discussed in the main text that

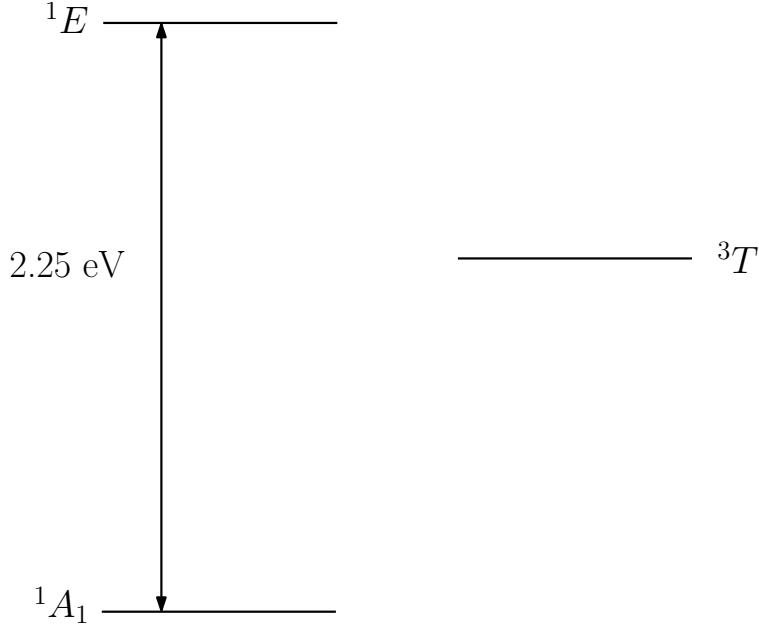


Figure S8: **Observed electronic structure of the ST1 defect.** Levels are labelled by their appropriate term symbols. Note that the orbital symmetries of  $^1E$  and  $^3T$  are unknown. The vertical arrow denotes the optical ZPL at 550 nm (2.25 eV). The estimate  $\sim 0.15$  eV obtained for the lattice relaxation energy in the previous section can be combined with the ZPL to estimate an energy of  $\sim 2.40$  eV between the  $^1A_1$  and  $^1E$  electronic levels. Other electronic levels may be present, but are yet to be detected.

the nuclear resonance of the  $^{13}\text{C}$  nuclear spin performed whilst the defect is in the electronic ground state implies that the ground electronic level is a spin singlet. These facts can be used to conclude various aspects of the defect's electronic structure.

According to Hund's rules, a spin singlet ground state can only occur if the ground electronic configuration is closed (i.e. filled electron orbitals) [20]. Using the electron orbital notation of figure S2, the ground electronic configuration is  $a^2$ , where all lower energy orbitals (i.e. orbitals of the valence band) are taken to be filled. Applying Unsold's theorem, a closed configuration is necessary orbitally symmetric (denoted  $A_1$ ) [20], such that the term symbol of the ground electronic level is  $^1A_1$ . Optical excitation promotes one of the electrons to the higher energy orbital  $b$ , such that the configuration of the optically excited level is  $ab$ . Spin selection rules of optical transitions imply that the optically excited state is also a spin singlet. As the symmetry of the orbitals are unknown, it is not possible to determine the orbital symmetry of the optically excited state, so for convenience it will be denoted by the term symbol  $^1E$ . The spin triplet level may be of the same configuration as  $^1E$  (the triplet being lower in energy in accordance with Hund's rules) or another excited configuration. Consequently, the orbital symmetry of the triplet level is also unknown and it will be labelled by the convenient term symbol  $^3T$ . There may also exist other electronic levels between the triplet and singlet levels and also above  $^1E$  (which are relevant as they may be populated under 532 nm excitation). However, such additional levels have not been detected thus far. The aspects of the electronic structure that can be concluded from our observations are depicted in figure S8. Future optical polarization and stress studies can be used to determine the orbital symmetry of the optically excited singlet level [2].

Given the observed aspects of the defect's electronic structure, a working model can be established of the defect's optical cycle (refer to figure S9). Beginning in the ground state, optical excitation transfers the defect into a vibronic level of  $^1E$ , which is followed by rapid non-radiative decay through the  $^1E$  vibronic levels, such that thermal equilibrium is established within the level's lifetime. From the  $^1E$  level, the defect may decay radiatively back to the ground state or non-radiatively via an intersystem crossing (ISC) to the

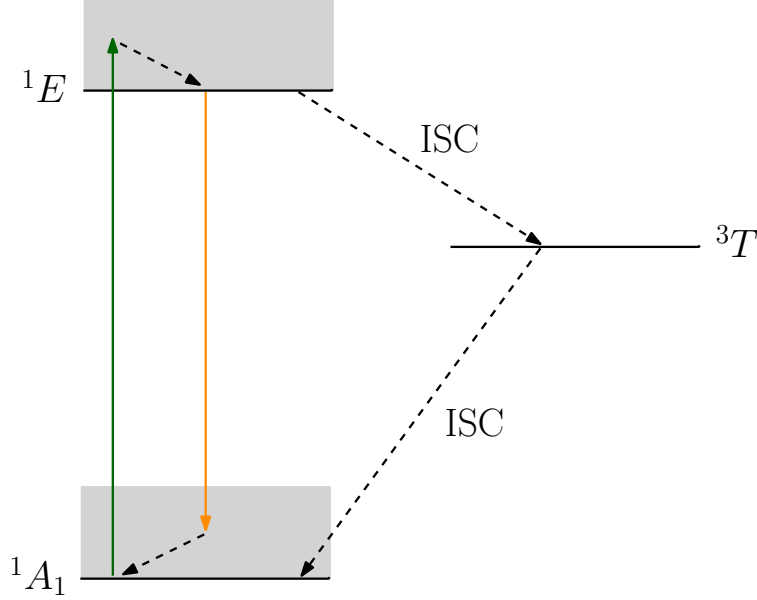


Figure S9: **Model of the optical cycle of the ST1 defect.** Known electronic levels are denoted by solid lines. The continuum of vibronic levels that give rise to the optical absorption and emission bands are depicted as shaded regions. Solid vertical arrows denote radiative transitions. Dashed arrows denote non-radiative decay within the vibronic levels of  $^1A_1$  and  $^1E$  as well as the ISCs between the singlet and triplet levels.

metastable triplet level. The defect decays from the  $^3T$  level by a subsequent ISC to the ground state. The ISCs are allowed via spin-orbit coupling of the triplet and singlet levels and are mediated by phonon emission [3]. The nature of spin-orbit coupling implies that the ISCs will be to some degree dependent on triplet spin-projection. The net effect being different storage times in the triplet level for different spin-projections that results in a modulation of the optical fluorescence if the defect is transferred between the spin-projections of the triplet. The presence of other electronic levels in the optical cycle will to some degree change the behavior of the cycle from that described by the model depicted in figure S9. No such variance has been detected to date.

## 5 Triplet level spin-Hamiltonian, zero-field splittings and spin axes

The spin-Hamiltonian that is appropriate to model the fine structure of the triplet level takes the general form [3, 15]

$$\hat{H} = \vec{S} \cdot \mathbf{D} \cdot \vec{S} + \vec{S} \cdot \mathbf{g} \cdot \vec{B} \quad (\text{S.9})$$

where  $\vec{S}$  is the dimensionless  $S = 1$  spin operator,  $\vec{B}$  is the magnetic field at the defect, and  $\mathbf{D}$  and  $\mathbf{g}$  are each  $3 \times 3$  tensors to be determined experimentally. The first term describes the effects of the crystal field that typically arise from electronic spin-spin interactions and/ or second-order spin-orbit interactions. The second term describes the electronic Zeeman interaction as governed by the tensor  $\mathbf{g}$ , which typically differs from the isotropic g-factor of a free-electron  $g_e = 2.0023$  by orbital angular momentum and spin-orbit effects.

By an appropriate choice of the defect coordinate system ( $xyz$ ), the crystal field tensor  $\mathbf{D}$  may be diagonalized. Furthermore, as our experiments did not detect any anisotropy in the electronic Zeeman interaction, the tensor  $\mathbf{g}$  may be reduced to an isotropic g-factor. The simplified spin-Hamiltonian is thus [3, 15]

$$\hat{H} = D[S_z^2 - S(S+1)/3] + E(S_x^2 - S_y^2) + g\vec{S} \cdot \vec{B} \quad (\text{S.10})$$

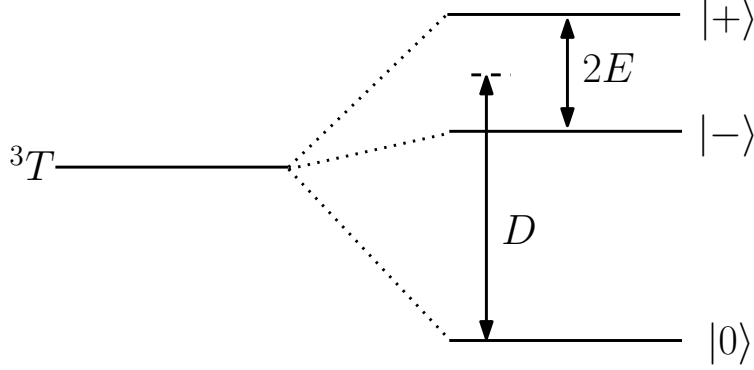


Figure S10: **Triplet level zero field fine structure.** Note that  $D$  and  $E$  have been assumed positive. In terms of the spin states  $|m_s\rangle$  with triplet spin-projection  $m_s$ , the zero field eigenstates are  $|+\rangle = (|+1\rangle + |-1\rangle)/\sqrt{2}$ ,  $|-\rangle = (|+1\rangle - |-1\rangle)/\sqrt{2}$  and  $|0\rangle$ .

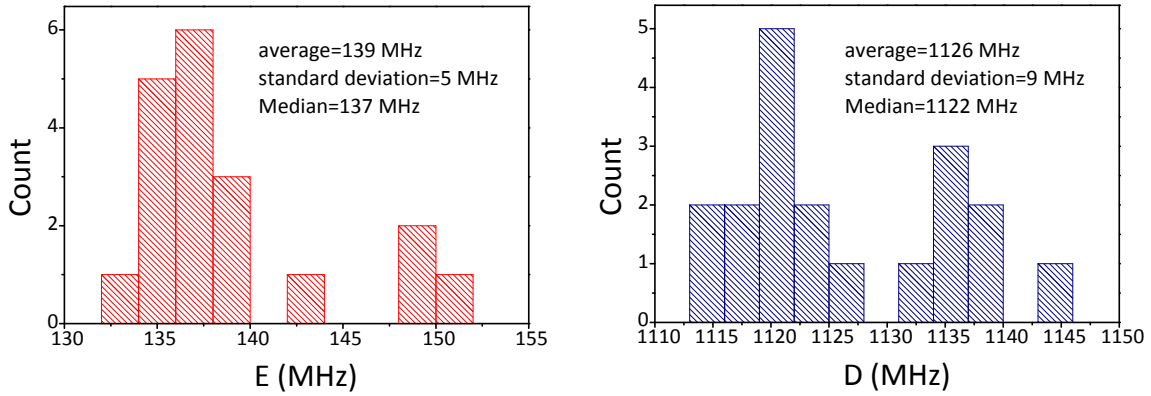


Figure S11: **Distributions of the ZFS of 19 ST1 defects.** The variance of the parameters is consistent with a distribution of strain within the nano-wires.

where  $D$  and  $E$  are zero field splitting (ZFS) parameters and  $g = 2.0(1)$  is the observed isotropic g-factor. The zero field fine structure of the triplet level that is described by the above spin-Hamiltonian is depicted in figure S10. The distributions of the observed ZFS parameters of 19 defects are shown in figure S11. The relatively small variance of the parameters strongly indicates that they are intrinsic properties of the ST1 defect that are slightly modified by the local strain of each defect site. Note that the imprecision of the observed g-factor is due to the experimental uncertainty of the magnetic field calibration. Also note that a precise measurement of the g-factor could give additional insight into the symmetry of the defect: Anisotropy of the g-factor arises due to spin-orbit coupling between the electronic levels and these couplings obey symmetry selection rules.  $C_{2v}$  symmetry implies negligible spin-orbit coupling and thus likely an isotropic g-factor, while in case of a symmetry lower than  $C_{2v}$ , an anisotropic g-factor could be present. The precise sign of the ZFS parameters can not be determined from our measurements.

The spin transition frequencies for different orientations of a static magnetic field are depicted in figure S12. The spin resonances have clear relationships when the magnetic field is aligned along one of the defect's coordinate axes. The orientation of the magnetic field can be simultaneously measured with respect to the crystal coordinate system using three inequivalent nearby  $NV^-$  centers and knowledge of their  $[111]$  symmetry axis (method described elsewhere [21]). Consequently, the ST1 defect's major ( $z$ ) axis was determined by

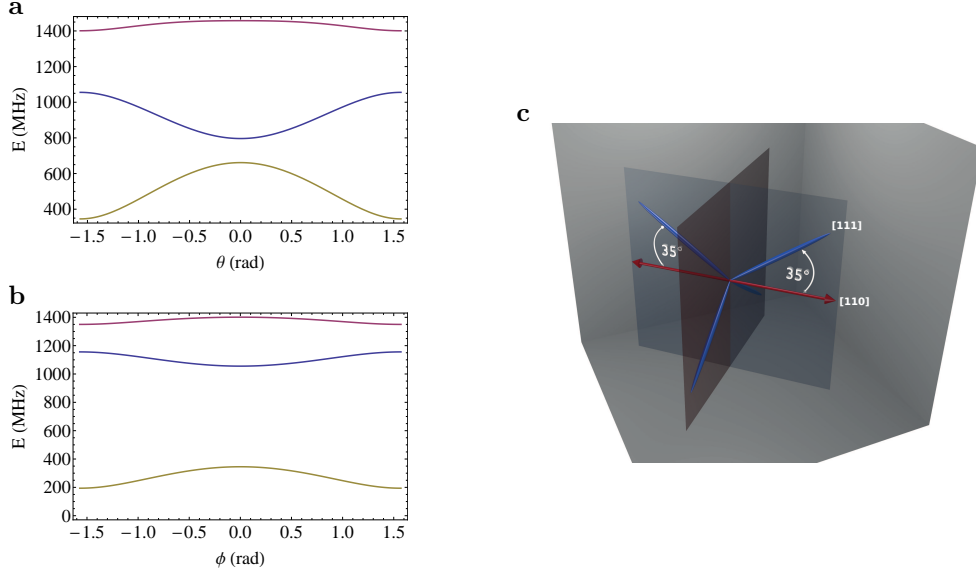


Figure S12: **Magnetic field alignment and major symmetry axis.** The plots depict the variation of the three spin resonances as a function of magnetic field orientation: (a)  $B_x = B \sin \theta$ ,  $B_y = 0$ ,  $B_z = B \cos \theta$ ; and (b)  $B_x = B \cos \phi$ ,  $B_y = B \sin \phi$ ,  $B_z = 0$ . The values  $D = 1128$  MHz,  $E = 139$  MHz and  $B = 300$  MHz were used to produce the plots. Relationships between the resonances are evident when the magnetic field is aligned with the defect's  $z$  axis ( $\theta = 0$ ),  $x$  axis ( $\phi = 0$ ) and  $y$  axis ( $\phi = \pi/2$ ). (c) Major symmetry axis of the ST1 defect. Blue lines indicate the four NV axes in the diamond crystal.

monitoring the ODMR frequencies of a chosen ST1 defect and nearby  $NV^-$  centers whilst manipulating the orientation of the magnetic field generated by an electromagnet placed above the sample. The elicited major axis together with the four  $NV^-$  orientations is shown in figure S12c. The major axis is on a plane defined by two  $NV^-$  axes (NV1 and NV2 axes in this plot) and off by  $35(1)^\circ$  with respect to these two axes and perpendicular to the other two  $NV^-$  axes. These findings lead to the conclusion that the major axis is approximately in the [110] crystal direction. The same conclusion has been obtained from several other ST1 defects.

The ZFS parameters of molecule-like defects in diamond, such as the  $NV^-$  center, are predominately due to spin-spin interactions, whereas the ZFS parameters of atom-like defects, such as transition metal ion impurities, arise largely from spin-orbit interactions [3, 15]. Assuming that the ZFS parameters arise from spin-spin interaction between the two unpaired electrons of the triplet level, the ZFS parameters provide insight into the distribution of unpaired spin density associated with the triplet level via the following expressions [15]

$$\begin{aligned}
 D &= \frac{3}{2} g_e^2 \frac{\mu_0}{4\pi} \langle \frac{1 - 3(z_{12}^2/r_{12}^2)}{r_{12}^3} \rangle \\
 E &= -\frac{3}{2} g_e^2 \frac{\mu_0}{4\pi} \langle \frac{x_{12}^2 - y_{12}^2}{r_{12}^5} \rangle
 \end{aligned}
 \tag{S.11}$$

where  $\mu_0$  is the vacuum permeability,  $\mu_B$  is the Bohr magneton,  $x_{12}$ ,  $y_{12}$ ,  $z_{12}$  are the coordinates of the displacement vector  $\vec{r}_{12}$  with magnitude  $r_{12}$  that connects the positions of the two electrons, and the angle brackets denote the direct integral over the unpaired spin density. Note that the exchange integral is neglected in the above.

The interpretation of the observed ZFS parameters of the ST1 defect using the above expressions indicates that the unpaired spin density is elongated along the major ( $z$ ) axis of the defect and is not symmetrical in the  $x - y$  plane of the defect [15]. To explain this interpretation, an analogy may be drawn with the

NV<sup>-</sup> center, where the ground state unpaired spin density is equally distributed over the three dangling sp<sup>3</sup> bonds of the carbon atoms surrounding the vacancy [3]. The trigonal symmetry of the NV<sup>-</sup> center implies that its ground state spin density is symmetrical in the (111) plane in the absence of strain, but is elongated along the [111] direction. The  $E$  parameter of NV<sup>-</sup> is therefore zero in the absence of strain, whilst the  $D$  parameter is non-zero. In the presence of strain, the trigonal symmetry of the NV<sup>-</sup> center is lowered and its ground state spin density is distorted in the (111) plane, thereby resulting in a non-zero  $E$  parameter. The non-zero  $E$  parameter of the ST1 defect implies that it is a defect of less than trigonal symmetry [3, 15]. Combining this conclusion with the orientation of the defect's major axis along the [110] direction restricts the set of possible point group symmetries of the ST1 defect to just including  $C_{2v}$  and its sub-groups:  $C_2$ ,  $C_{1h}$ , and  $C_1$ .

The value of  $D$  for the ST1 defect may also be used to crudely estimate an upper bound of 4 angstroms for the average separation  $\langle r_{12} \rangle$  of the two unpaired electrons [3, 15]. A similar estimate applied to the ground state of the NV<sup>-</sup> center yields 3 angstroms [5]. By comparison, it can be concluded that the spin density of the ST1 defect is likely to be distributed over a greater region than the ground state spin density of the NV<sup>-</sup> center. The ZFS parameters are thus consistent with an unpaired spin density distributed over the orbitals of several atomic sites along the [110] crystal direction. The ZFS parameters are thus consistent with some degree of preferential distribution of the unpaired spin density over the orbitals of several atomic sites along the [110] crystal direction.

## 6 Triplet hyperfine structure

Two of the ST1 defects studied exhibited hyperfine structure of the triplet level due to magnetic interactions with a <sup>13</sup>C nucleus. One of them showed a particularly large hyperfine splitting greater than 100 MHz and was used throughout this work (refer to figure 4 main text). Figure S13 shows the hyperfine splittings of this defect in the vicinity of a level-anti-crossing between the  $|0\rangle$  and  $|-1\rangle$  electronic spin manifolds. These interactions are described by the addition of the following term to the triplet spin-Hamiltonian (S.10) [3, 15]

$$V_{hf} = \vec{S} \cdot \mathbf{A} \cdot \vec{I} \quad (\text{S.12})$$

where  $\vec{I}$  is the dimensionless  $I = 1/2$  nuclear spin operator and  $\mathbf{A}$  is a  $3 \times 3$  tensor to be determined experimentally. With an appropriate choice of nuclear spin coordinate system ( $XYZ$ ), the tensor  $\mathbf{A}$  may be diagonalized, simplifying the above to [3, 15]

$$V_{hf} = A_{xx}S_xI_X + A_{yy}S_yI_Y + A_{zz}S_zI_Z \quad (\text{S.13})$$

Note that the nuclear spin coordinate system ( $XYZ$ ) is in general different to the defect's coordinate system ( $xyz$ ). Figure S14 depicts the triplet hyperfine structure at zero field and in the presence of a static magnetic field aligned along the defect's major axis ( $B_z$ ) (nuclear Zeeman interaction ignored). At zero field, the hyperfine structure is suppressed by the effects of the crystal field parameter  $E$  (refer to figure 4 main text). The observed hyperfine resonances as functions of  $B_z$  (data shown in figure S13), together with their least squares best fit obtained using the spin-Hamiltonian model, are depicted in figure S15. The fitted values of the various spin-Hamiltonian parameters are contained in table S3. Note that no difference could be detected between the hyperfine parameters  $A_{xx}$  and  $A_{yy}$ , such that they both can be equated to a single parameter  $A_{\perp} = A_{xx} = A_{yy}$ .

$D$ (MHz)	$E$ (MHz)	$A_{zz}$ (MHz)	$A_{\perp}$ (MHz)
1134.7(7)	139(2)	-117(1)	-94(2)

Table S3: **Triplet level hyperfine parameters.** The parameters are those of the single ST1 defect whose hyperfine structure was studied in figure S15. Note that  $A_{xx} = A_{yy} = A_{\perp}$ .

The hyperfine parameters can be used to interpret the character of the unpaired electronic spin density distribution at the <sup>13</sup>C nucleus. The magnetic hyperfine interaction contains distinct Fermi contact  $f$  and

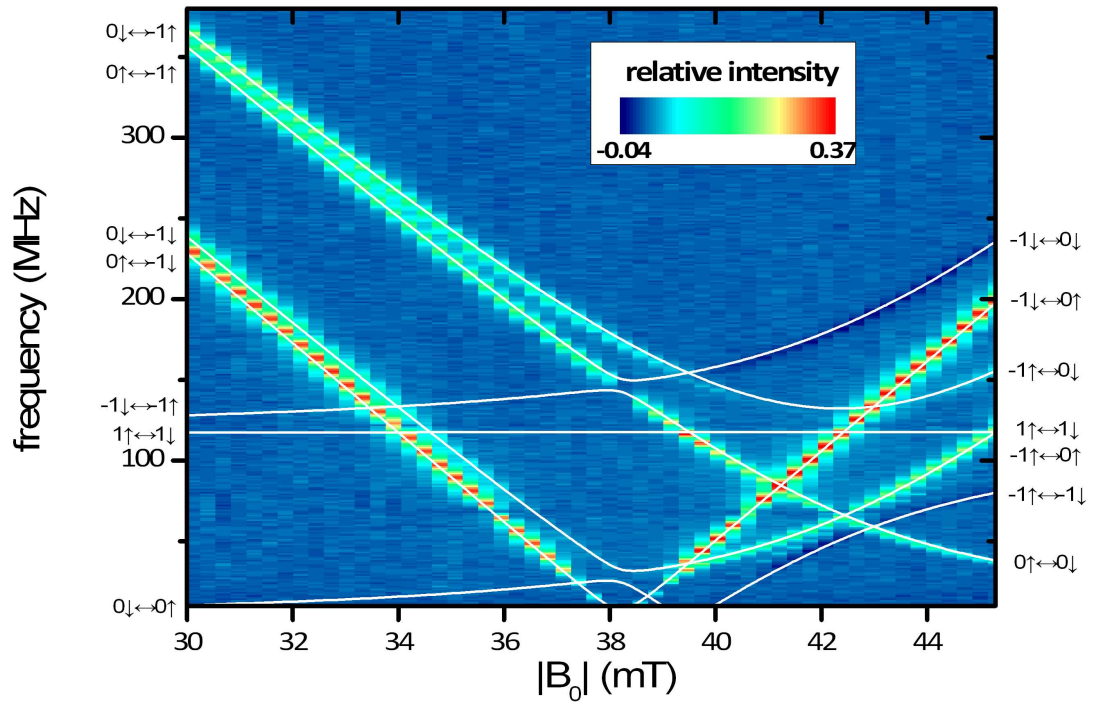
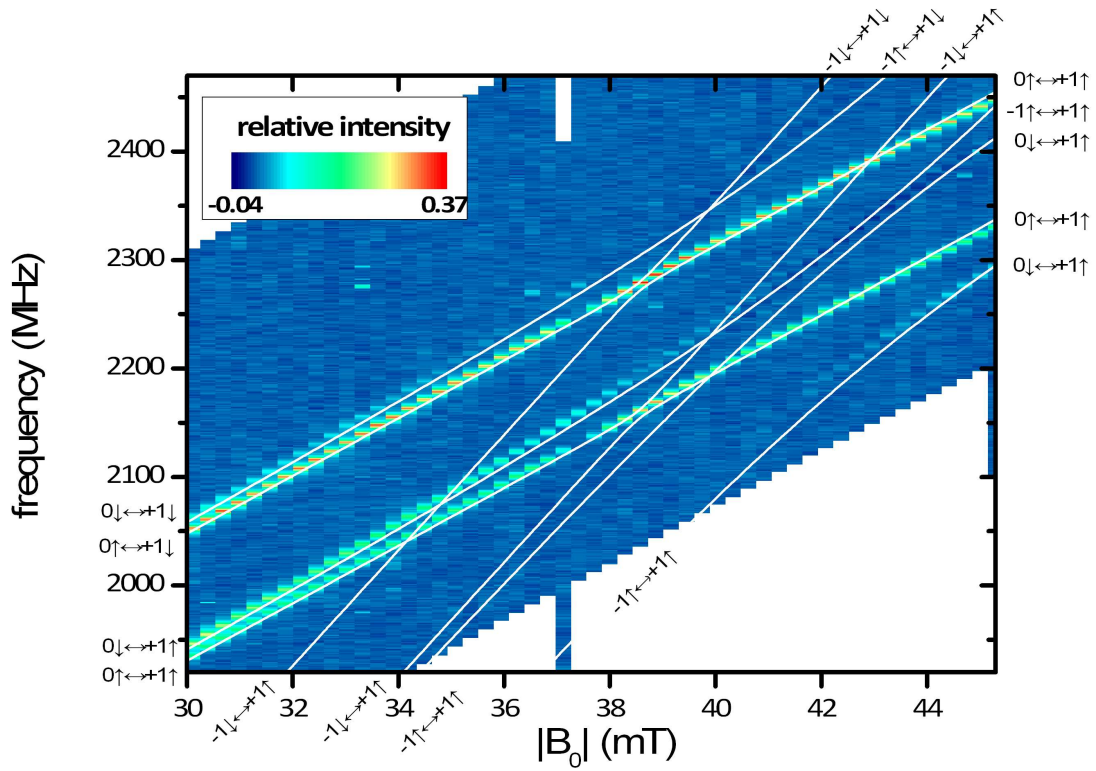


Figure S13: **Hyperfine structure at the LAC.** Upper panel:  $D + E$  transition, lower panel:  $D - E$  transition. The color maps show experimental ODMR data. White lines show theoretical results. The approximate eigenstates linking the transitions are denoted on the sides of the plots.

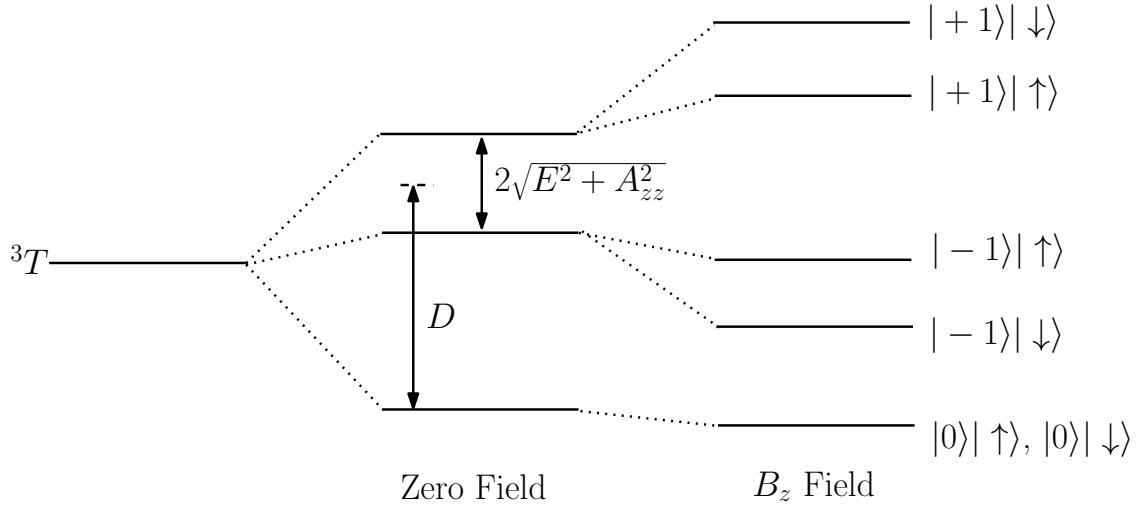


Figure S14: **Triplet level hyperfine structure.** The zero field energies are correct to first order in the hyperfine interaction. The approximate eigenstates in the presence of an aligned magnetic field fulfilling  $B_z \gg E$  are expressed in terms of the electronic spin states ( $|m_s\rangle$ ), where  $m_s$  denotes electronic spin-projection, and the nuclear spin states ( $|\uparrow\rangle, |\downarrow\rangle$ ), where up/ down arrows denote  $m_I = +\frac{1}{2}/ -\frac{1}{2}$  nuclear spin projections.

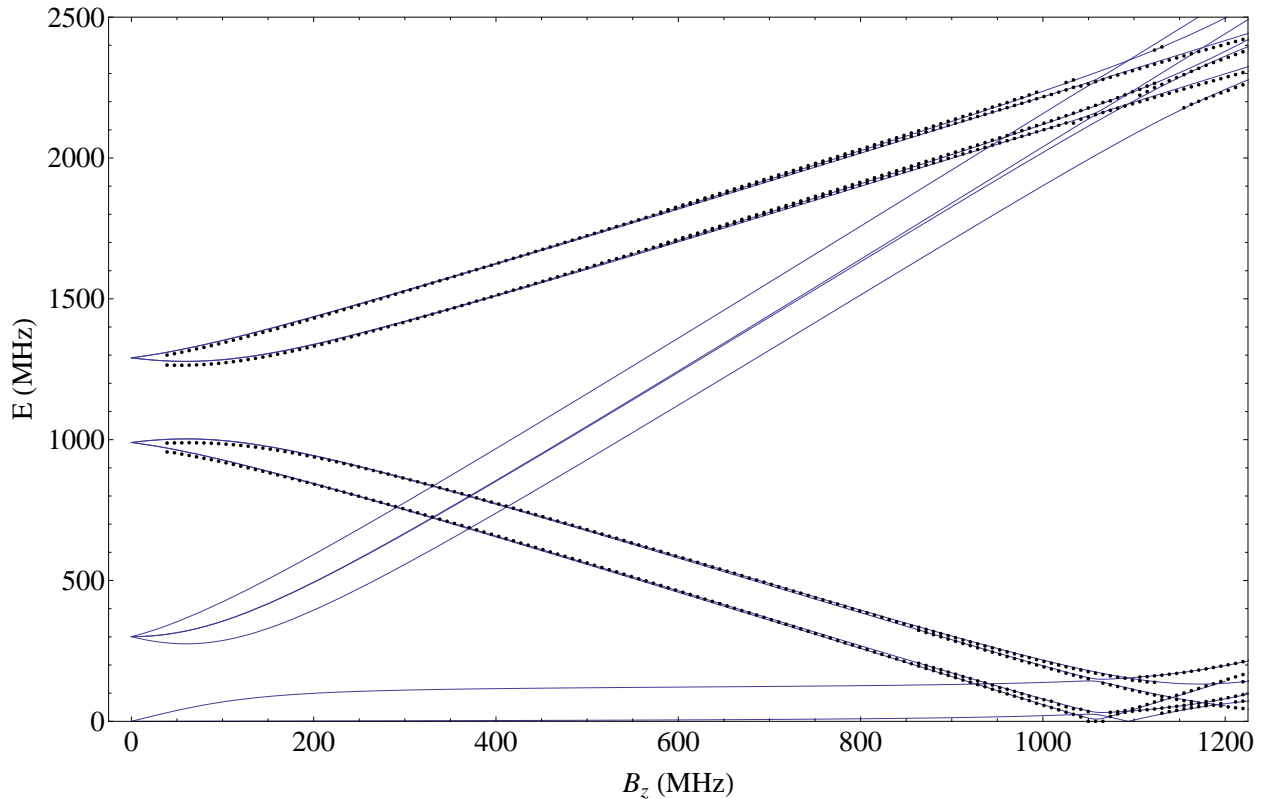


Figure S15: **Triplet hyperfine resonances as functions of  $B_z$ .** Solid lines denote the resonant frequencies described by the spin-Hamiltonian model (S.10, S.12). Points denote the observed resonant frequencies.

dipolar  $d$  terms, such that [3, 5]

$$\begin{aligned} A_{zz} &= f + d \\ A_{\perp} &= f - 2d \end{aligned} \quad (\text{S.14})$$

Using the fitted values of  $A_{zz}$  and  $A_{\perp}$  contained in table S3, the values  $f = -101(2)$  MHz and  $d = -7.8(9)$  MHz can be determined. The electronic orbitals  $\psi$  that comprise the unpaired spin density associated with the  $^{13}\text{C}$  atom can be well described by linear combinations of  $2s$  ( $\phi_s$ ) and  $2p$  ( $\phi_p$ ) atomic orbitals [3, 5]

$$\psi = c_s \phi_s + c_p \phi_p \quad (\text{S.15})$$

where  $c_s$  and  $c_p$  are coefficients that satisfy the normalization condition  $1 = |c_s|^2 + |c_p|^2$ . The Fermi contact and dipolar terms may be expressed in terms of the orbital coefficients and the portion of unpaired spin density  $\eta$  contributed by the atomic orbitals of the  $^{13}\text{C}$  atom via [3, 5]

$$\begin{aligned} f &= \frac{8\pi}{3} \frac{0}{4\pi} g_e B g_n \eta |c_s|^2 |\phi_s(0)|^2 \\ d &= \frac{2}{5} \frac{0}{4\pi} g_e B g_n \eta |c_p|^2 \langle \phi_p | \frac{1}{r^3} | \phi_p \rangle \end{aligned} \quad (\text{S.16})$$

where  $g_n$  is the  $^{13}\text{C}$  nuclear g-factor,  $n$  is the nuclear magneton,  $\phi_s(0)$  is the value of the  $2s$  orbital at the nucleus and  $r$  is the distance of the electron spin from the nucleus. As per established practice in the electron spin resonance of defects in diamond [3, 15, 5, 22], the values of  $|\phi_s(0)|^2$  and  $\langle \phi_p | \frac{1}{r^3} | \phi_p \rangle$  obtained from self-consistent field calculations of atomic carbon can be used in conjunction with the observed values of  $f$  and  $d$  to estimate  $|c_s|^2$ ,  $|c_p|^2$  and  $\eta$ . The estimated values are 0.27, 0.73 and 0.1, respectively.

The estimated values of  $|c_s|^2$  and  $|c_p|^2$  are very close to the values of a standard  $\text{sp}^3$  bonding orbital of diamond, being 0.25 and 0.75, respectively. Consequently, it appears that the spin density at the  $^{13}\text{C}$  site of this particular ST1 defect occupies a typical  $\text{sp}^3$  orbital. Furthermore, only  $\sim 10\%$  of the spin density is associated with that site, implying that the spin density is distributed over a number of atomic sites. This conclusion, when combined with the observed  $\sim 1$  MHz ODMR linewidths and typical hyperfine interaction energies, implies that if the defect possessed an intrinsic nuclear spin it would most likely have been detected. Hence, it may also be conservatively concluded that the defect does not possess an intrinsic nuclear spin.

## 7 Defect structure

Summarising previous sections, the properties of the ST1 defect structure that we may conclude from our observations are:

- The optical transition occurs between energetically discrete electron orbitals within the diamond bandgap and is accompanied by an appreciable lattice relaxation.
- The ground and optical excited electronic levels are spin singlets
- There exists a metastable spin triplet level between the singlet levels
- The triplet level's major axis is in the [110] direction.
- The defect has  $C_{2v}$  or lower point group symmetry.
- The defect does not contain an intrinsic impurity that possesses a nuclear spin.
- The mean separation of the unpaired electrons of the triplet level is less than 4 angstroms.
- The unpaired spin density is distributed over a number of atomic sites.

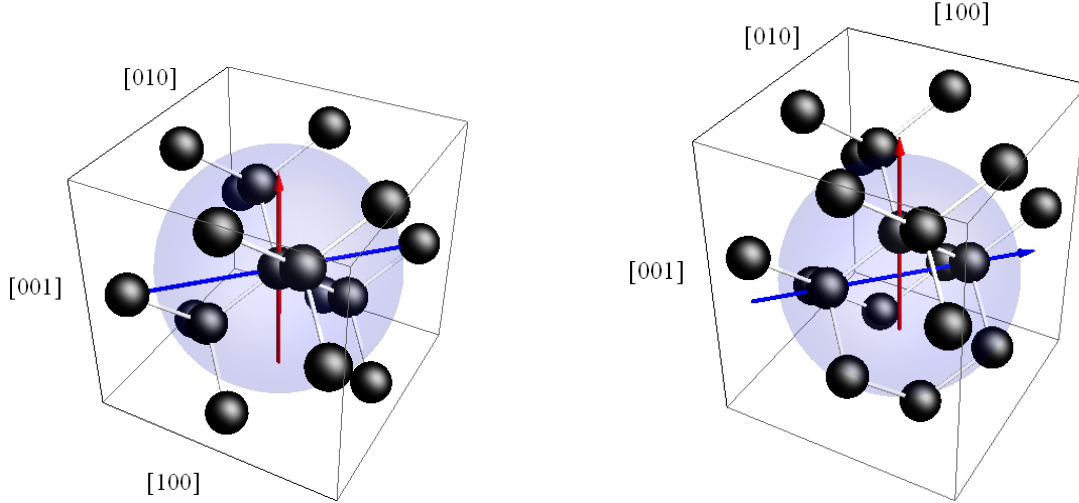


Figure S16: **Possible regions of the diamond lattice occupied by the ST1 defect.** The diagrams depict two portions of the diamond crystal structure: (a) a portion centered on an atomic site and (b) a portion centered on the midpoint between two atomic sites along the  $[110]$  direction. The transparent sphere in each diagram has a diameter of 4 angstroms and indicates the region where the unpaired spin density of the triplet level is localized. The red arrow denotes the  $C_2$  symmetry axis of the  $[110]$  direction and the blue arrow is parallel to the  $[110]$  direction. The plane formed by the  $C_2$  symmetry axis and the  $[110]$  direction is the reflection plane of the diamond lattice corresponding to the  $[110]$  direction. Black spheres represent atomic sites and white tubes denote  $sp^3$  bonds.

- 10% of the unpaired spin density is located at one particular carbon site and has the character of a  $sp^3$  orbital.

Figure S16 depicts two portions of the diamond crystal structure: one portion is centered on an atomic site and the other portion is centered on the midpoint between two atomic sites along the  $[110]$  direction. The transparent sphere in each diagram has a diameter of 4 angstroms and thus indicates the region where the unpaired spin density of the triplet level is localized, if the defect is atom centered or midpoint centered. Consistent with our observations, it is clear that for both cases, there exist several atomic sites (up to 7) within the region where the spin density is localized.

The conclusion that the defect does not contain an intrinsic impurity that possesses a nuclear spin restricts the set of possible constituents of the defect. The restricted set contains substitutional and interstitial impurities without nuclear spins, as well as the structural defects of diamond: the vacancy and self-interstitial. The defect is likely to be a complex of these possible constituents, although given the relatively small region where the spin density is localized, it is probable that it contains only up to two or three. The simplest structure of the defect that is consistent with our observations is a pair of constituents occupying atomic or interstitial sites along the  $[110]$  direction. A pair of the same constituent will form a defect with the highest possible  $C_{2v}$  symmetry if they are both occupying atomic or interstitial sites. The pair of different constituents will form a defect with  $C_{1h}$  symmetry. More complicated complexes can form defects with  $C_2$  and  $C_1$  symmetry.

Due to the involved fabrication process of the nano-wires, it is not possible to further restrict the set of possible constituents of the defect. Systematic formation studies are required to gain more information about the constituents. Given that oxygen plasma was used during the reactive ion etching process, it is capable of  $sp^3$  bonding and the abundant  $^{16}O$  isotope does not have a nuclear spin, the presence of  $^{16}O$  in the defect is certainly possible and warrants further investigation. The significant strain that is likely to be present in the nano-wires potentially plays a significant role in the formation energetics of the ST1 defect and may explain why the defect has not been previously observed in bulk diamond.

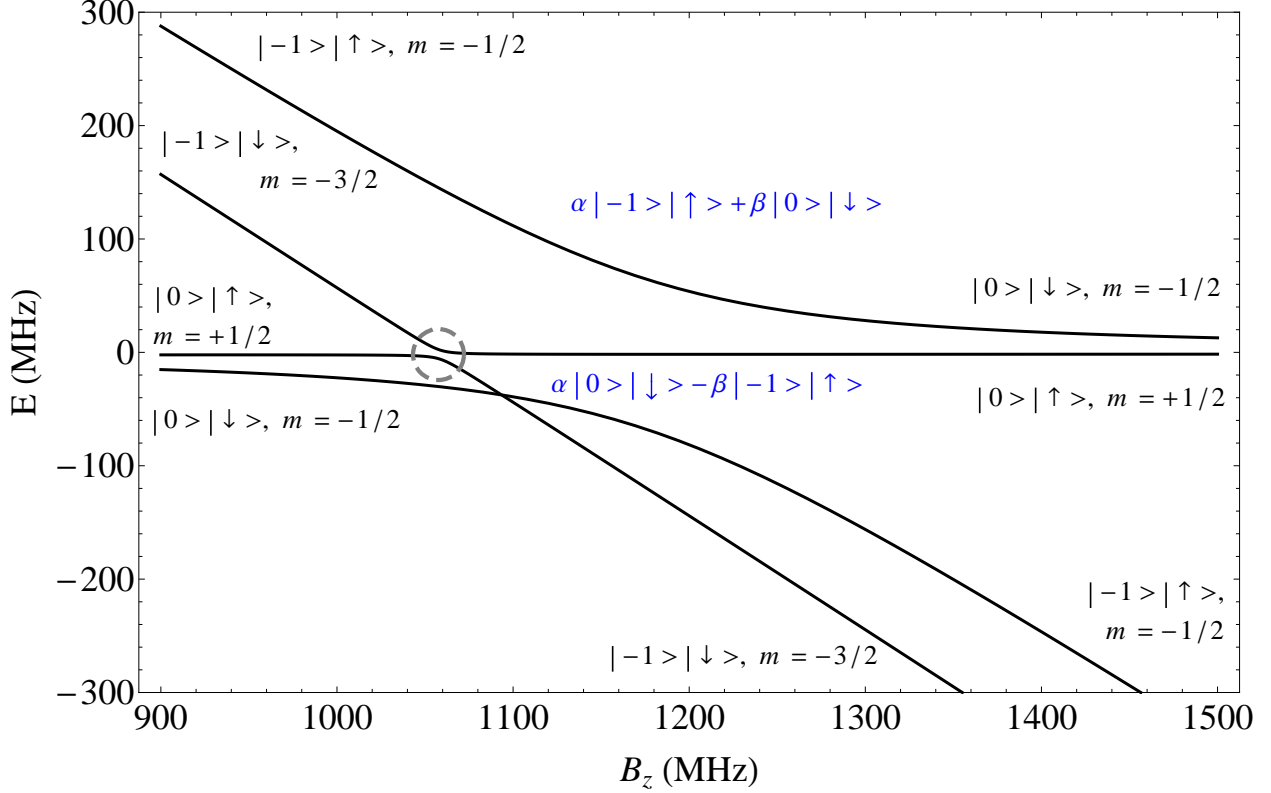


Figure S17: **The triplet level hyperfine level anti-crossing.** Solid lines denote the hyperfine energy levels in the region of the LAC. The approximate states and electro-nuclear spin projection  $m$  of the levels before and after the LAC are depicted in black. The mixed states of the  $m = -1/2$  levels at the LAC are depicted in blue. The dashed circle highlights the minor LAC between the  $m = +1/2$  and  $-3/2$  levels discussed in the text.

## 8 Nuclear spin polarization and readout

The hyperfine structure of the ST1 defect discussed in section 6 exhibits a level anti-crossing (LAC) in the region of a static magnetic field of strength  $B_z \sim 42$  mT that is aligned along the defect's major axis (refer to figure S17). Since  $B_z$  and  $D$  are the dominate terms of the spin-Hamiltonian near the LAC, the electro-nuclear spin projection  $m = m_s + m_I$  is an approximately good quantum and the levels in figure S17 have been labelled accordingly. In the region of the LAC, the transverse hyperfine terms  $A_{\perp}$  mix levels of the same spin projection  $m$ , such that the levels with  $m = -\frac{1}{2}$  are mixed, but the levels with  $m = +\frac{1}{2}$  and  $-\frac{3}{2}$  are approximately unmixed. Strictly, the  $m = +\frac{1}{2}$  and  $-\frac{3}{2}$  levels do undergo a small LAC (as indicated in figure S17) induced by the relatively small  $E$  terms. The  $\bar{E}$  term and anisotropic hyperfine coupling also result in small admixtures of the  $|+1, \pm 1/2\rangle$  hyperfine levels to the eigenstates near the LAC. We proceed by formulating a basic model, where we neglect the  $E$  term and assume isotropic hyperfine coupling. In this case, the mixed states are composed from only two components  $|-1, +1/2\rangle$  and  $|0, -1/2\rangle$  (total spin  $m = -\frac{1}{2}$ ) and they can be quantified by the coefficients  $\alpha$  and  $\beta$  (with  $|\alpha|^2 + |\beta|^2 = 1$ ) as denoted in figure S17.

We now use this hamiltonian to construct a basic 10-level rate-equation model that describes nuclear spin polarization by optical pumping and optical nuclear spin readout[8, 9]. We first neglect electronic spin relaxation and assume that the population rates of each of the triplet electronic spin states are equal. This remaining transitions are summarized in figure S18. To simplify the notation, we denote the triplet

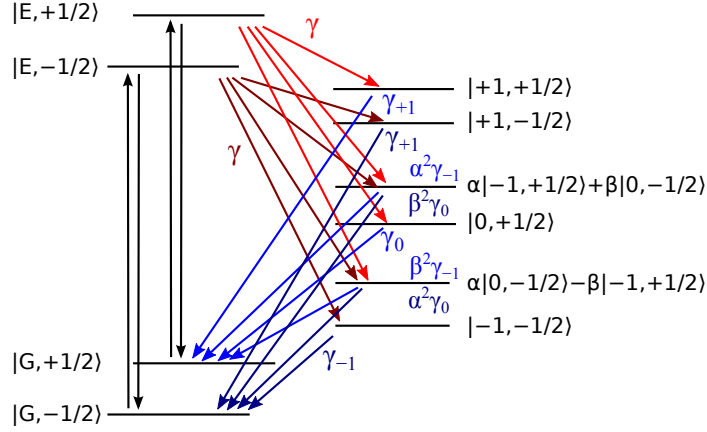


Figure S18: 10-level rate equation model for optical nuclear spin polarization and readout.

population rate far away from the LAC by  $\gamma$  and the decay rates out of the electronic triplet states  $\gamma_0$ ,  $\gamma_{-1}$ ,  $\gamma_{+1}$ . The population and decay rates of the unmixed states are

$$\begin{aligned}
 |E, \pm 1/2\rangle &\rightarrow |+1, \pm 1/2\rangle : \gamma \\
 |E, +1/2\rangle &\rightarrow |0, +1/2\rangle : \gamma \\
 |E, -1/2\rangle &\rightarrow |-1, -1/2\rangle : \gamma \\
 |+1 \pm 1/2\rangle &\rightarrow |G, \pm 1/2\rangle : \gamma_{\pm 1} \\
 |0, +1/2\rangle &\rightarrow |G, +1/2\rangle : \gamma_0 \\
 |-1, -1/2\rangle &\rightarrow |G, -1/2\rangle : \gamma_{-1}
 \end{aligned} \tag{S.17}$$

The transitions rates for the mixed states  $|I\rangle = \alpha|-1, +1/2\rangle + \beta|0, -1/2\rangle$  and  $|II\rangle = \alpha|0, -1/2\rangle - \beta|-1, +1/2\rangle$  are easily found by considering the matrix elements of the transition operator  $D$ . For example the decay rate from  $|I\rangle$  to ground state  $+1/2$  is found as

$$\begin{aligned}
 \gamma_{|I\rangle|G,+1/2\rangle} &= |\langle G, +1/2|D(\alpha|-1, +1/2\rangle + \beta|0, -1/2\rangle)|^2 \\
 &= |\alpha\langle G, +1/2|D|-1, +1/2\rangle + \beta\langle G, +1/2|D|0, -1/2\rangle|^2 \\
 &= |\alpha\langle G, +1/2|D|-1, +1/2\rangle|^2 = |\alpha|^2\gamma_{-1}
 \end{aligned} \tag{S.18}$$

The population and decay rates of the mixed states are thus

$$\begin{aligned}
 |E, +1/2\rangle &\rightarrow \alpha|-1, +1/2\rangle + \beta|0, -1/2\rangle : |\alpha|^2\gamma \\
 |E, -1/2\rangle &\rightarrow \alpha|-1, +1/2\rangle + \beta|0, -1/2\rangle : |\beta|^2\gamma \\
 |E, +1/2\rangle &\rightarrow \alpha|0, -1/2\rangle - \beta|-1, +1/2\rangle : |\beta|^2\gamma \\
 |E, -1/2\rangle &\rightarrow \alpha|0, -1/2\rangle - \beta|-1, +1/2\rangle : |\alpha|^2\gamma \\
 \alpha|-1, +1/2\rangle + \beta|0, -1/2\rangle &\rightarrow |G, +1/2\rangle : |\alpha|^2\gamma_{-1} \\
 \alpha|-1, +1/2\rangle + \beta|0, -1/2\rangle &\rightarrow |G, -1/2\rangle : |\beta|^2\gamma_0 \\
 \alpha|0, -1/2\rangle - \beta|-1, +1/2\rangle &\rightarrow |G, +1/2\rangle : |\beta|^2\gamma_{-1} \\
 \alpha|0, -1/2\rangle - \beta|-1, +1/2\rangle &\rightarrow |G, -1/2\rangle : |\alpha|^2\gamma_0
 \end{aligned} \tag{S.19}$$

Spin polarization proceeds in two steps. First, we perform optical pumping until steady state is reached. Thereafter the system is allowed to decay to the ground state. Before we evaluate the numerical solution to the rate-equations, we provide a qualitative argument and consider the case at the center of the LAC, where  $\alpha = \beta = 2^{-1/2}$ . Under this condition, the total population rates of all triplet hyperfine states are equal. Thus, the steady state population is determined by the decay rates. Specifically, population will be trapped predominantly in the longest lived hyperfine level. The lifetimes  $\tau_i = 1/\gamma_i$  of the triplet states are

$$\begin{aligned}
|+1, \pm 1/2\rangle &: \gamma_{\pm 1}^{-1} \approx 200ns \\
\alpha|-1, +1/2\rangle + \beta|0, -1/2\rangle &: (1/2\gamma_0 + 1/2\gamma_{-1})^{-1} \approx 1400ns \\
|0, +1/2\rangle &: \gamma_0^{-1} \approx 2500ns \\
\alpha|0, -1/2\rangle + \beta|-1, +1/2\rangle &: (1/2\gamma_0 + 1/2\gamma_{-1})^{-1} \approx 1400ns \\
|-1, -1/2\rangle &: \gamma_{-1}^{-1} \approx 1000ns
\end{aligned} \tag{S.20}$$

The  $|+1 \pm 1/2\rangle$  states do not contribute imbalance of the decay rates for the  $+1/2$  and  $-1/2$  nuclear spin manifolds and can be ignored. The role of the mixed states is twofold. First, they provide nuclear spin flip transitions, and second, due to their larger decay rates to the  $+1/2$  ground state (see above), they result in an overall increased rate from the  $-1/2$  to the  $+1/2$  manifold. The unmixed states provide nuclear spin polarization by their different lifetimes. Specifically, population will accumulate predominantly in the long lived state  $|0, +1/2\rangle$ . Both mechanisms act in the same direction, such that, in the steady state under strong optical pumping, the largest fraction of the population will be in  $|0, +1/2\rangle$ , a relatively large population will also be in the mixed states, minor population will be in the  $|-1, +1/2\rangle$  state and negligible population in the  $|+1, \pm 1/2\rangle$  states. During a subsequent decay (after the pump laser is turned off), all population from the  $|0, +1/2\rangle$  will decay to the  $+1/2$  ground state and the mixed states will preferentially decay into the  $+1/2$  ground state. This will further increase the nuclear spin polarization. This process is described in terms of the change in the two ground state populations during a pulse sequence in figure S19. A full numerical analysis predicts a nuclear spin polarization  $(n_{+1/2} - n_{-1/2})/(n_{+1/2} + n_{-1/2}) \approx 60\%$ .

We now consider nuclear spin readout. Starting from ground state  $+1/2$  or ground state  $-1/2$ , we apply optical pumping until steady state is reached and evaluate the integrated fluorescence, that is given by the excited state populations (multiplied by the optical decay rate). The nuclear spin states will have different probability to be trapped in the long lived shelving state  $|0, +1/2\rangle$  and thus have a different overall fluorescence intensity. The mixed states do not contribute to readout contrast, since their population rates are equal and as soon as they are populated, the nuclear spin information is lost. Likewise, the  $|+1, \pm 1/2\rangle$  states do not contribute to readout contrast and the only relevant states are the two unmixed states. Appreciating the lifetimes evaluated in Eq.(S.20), we expect that the nuclear spin  $|G, +1/2\rangle$  will correspond to low fluorescence. A full numerical analysis predicts a fluorescence contrast between  $|G, +1/2\rangle$  and  $|G, -1/2\rangle$  of about 7%. The numerical analysis also predicts that the time to reach steady state is about  $6 - 8\mu s$ , as observed in experiment.

We now combine the results for nuclear spin polarization and readout contrast. The nuclear spin signal will be the product of both efficiencies. From this we expect a signal contrast of about 4%. This slightly overestimates the experimentally observed contrast of about 1.5%. This likely reflects the approximations made in this basic model. Next, we can consider the sign of the signal contrast contrast. Experimentally, we observe a maximum of the nuclear Rabi oscillations at zero microwave pulse length, indicating that the nuclear spin state that we polarize in corresponds to bright fluorescence. By contrast, the basic model suggests the opposite case, where the polarized state ( $|0, +1/2\rangle$ ) corresponds to low fluorescence. This is likely also a result of the simplifications made in above basic model.

Several aspects are likely to be relevant in a full description of the nuclear spin polarization- and readout contrast. One aspect is the small admixture from the  $|+1 \pm 1/2\rangle$  states into the eigenstates at the LAC. Due to the comparably fast decay rate of the these states, the relatively small admixture might become relevant. A second aspect are possible small differences among the population rates. While these are not important for the electron spin polarization, here they could become relevant. After designing a precise measurement for the population rates far away from the LAC, these could be included in a complete rate model. Lastly,

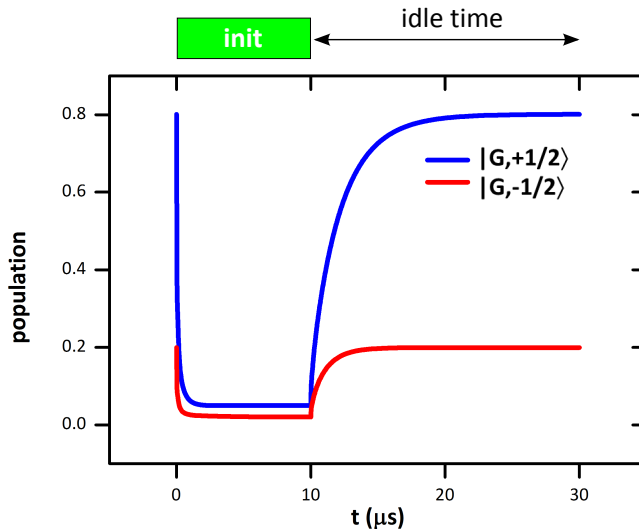


Figure S19: **Build-up of population in the ground state.** Each curve represents the time-evolution of two nuclear spin state populations during a pulse cycle. Note that 60 % polarization is already achieved after the first cycle (not shown) and this plots shows a time-evolution after many cycles.

electron-spin relaxation might be considered. Electron-spin relaxation would result in additional transition rates among the triplet hyperfine levels.

## References

- [1] G Davies. Vibronic spectra in diamond. *Journal of Physics C: Solid State Physics*, 7(20):3797–3809, October 1974.
- [2] G. Davies and M. F. Hamer. Optical Studies of the 1.945 eV Vibronic Band in Diamond. *Proceedings of the Royal Society of London. Series A, Mathematical and Physical Sciences and Physical Sciences*, 348(1653):285–298, 1976.
- [3] J H N Loubser and J A van Wyk. Electron spin resonance in the study of diamond. *Reports on Progress in Physics*, 41(8):1201–1248, August 1978.
- [4] A T Collins, M F Thomaz, and M I B Jorge. Luminescence decay time of the 1.945 eV centre in type Ib diamond. *Journal of Physics C: Solid State Physics*, 16(11):2177–2181, April 1983.
- [5] Xing-Fei He, Neil Manson, and Peter Fisk. Paramagnetic resonance of photoexcited N-V defects in diamond. I. Level anticrossing in the 3A ground state. *Physical Review B*, 47(14):8809–8815, April 1993.
- [6] A. Gruber. Scanning Confocal Optical Microscopy and Magnetic Resonance on Single Defect Centers. *Science*, 276(5321):2012–2014, June 1997.
- [7] A. Dräbenstedt, L Fleury, C Tietz, F Jelezko, S Kilin, A Nizovtzev, and J Wrachtrup. Low-temperature microscopy and spectroscopy on single defect centers in diamond. *Physical Review B*, 60(16):11503–11508, October 1999.

- [8] D. Stehlik, A Doehring, J.P. Colpa, E. Callaghan, and S. Kesmarky. Optical nuclear polarization in molecular crystals through an optical excitation cycle. *Chemical Physics*, 7(2):165–186, February 1975.
- [9] J.P. Colpa and D. Stehlik. Optical nuclear polarization as a consequence of the non-crossing rule (level-anti-crossing). *Chemical Physics*, 21(2):273–288, April 1977.
- [10] E.C. Reynhardt and C.J. Terblanche. <sup>13</sup>C relaxation in natural diamond. *Chemical Physics Letters*, 269(5-6):464–468, May 1997.
- [11] E.C Reynhardt and G.L High. Nuclear magnetic resonance studies of diamond. *Progress in Nuclear Magnetic Resonance Spectroscopy*, 38(1):37–81, January 2001.
- [12] Birgit J.M. Hausmann, Mughees Khan, Yinan Zhang, Tom M. Babinec, Katie Martinick, Murray McCutcheon, Phil R. Hemmer, and Marko Lončar. Fabrication of diamond nanowires for quantum information processing applications. *Diamond and Related Materials*, 19(5-6):621–629, May 2010.
- [13] Thomas M Babinec, Birgit J M Hausmann, Mughees Khan, Yinan Zhang, Jeronimo R Maze, Philip R Hemmer, and Marko Loncar. A diamond nanowire single-photon source. *Nature nanotechnology*, 5(3):195–9, March 2010.
- [14] K Iakoubovskii and G.J Adriaenssens. Optical characterization of natural Argyle diamonds. *Diamond and Related Materials*, 11(1):125–131, January 2002.
- [15] A M Stoneham. *Theory of Defects in Solids: Electronic Structure of Defects in Insulators and Semiconductor*. Oxford Classic Texts in the Physical Sciences Series. Clarendon Press, 2001.
- [16] G Davies. The Jahn-Teller effect and vibronic coupling at deep levels in diamond. *Reports on Progress in Physics*, 44(7):787–830, July 1981.
- [17] R W H Stevenson. *Phonons in perfect lattices and in lattices with point imperfections*. Scottish Universities’ Summer School. Oliver & Boyd, 1966.
- [18] Pierre A Chiha and Richard H Clarke. Triplet-state intersystem crossing rates from optically detected magnetic resonance spectroscopy. *Journal of Magnetic Resonance (1969)*, 29(3):535–543, March 1978.
- [19] W H Press, B P Flannery, S A Teukolsky, and W T Vetterling. *Numerical Recipes in FORTRAN 77: The Art of Scientific Computing*, volume 1. Cambridge University Press, 2nd edition, 1992.
- [20] M Tinkham. *Group Theory and Quantum Mechanics*. Dover Books on Chemistry Series. Dover, 1964.
- [21] S Steinert, F Dolde, P Neumann, a Aird, B Naydenov, G Balasubramanian, F Jelezko, and J Wrachtrup. High sensitivity magnetic imaging using an array of spins in diamond. *The Review of scientific instruments*, 81(4):043705, April 2010.
- [22] P B Ayscough. *Electron spin resonance in chemistry*. Number v. 1 in Electron Spin Resonance in Chemistry. Methuen, 1967.